










Spectroscopy of AT 2016blu’s recurring supernova impostor outbursts

Mojgan Aghakhanloo ¹*, Nathan Smith ², Jennifer E. Andrews ³, Alexei V. Filippenko ⁴,
Griffin Hosseinzadeh ⁵, Jacob E. Jencson ⁶, Jeniveve Pearson ², David J. Sand ²
Thomas G. Brink ⁴, Kelsey I. Clubb ⁴

¹ Department of Astronomy, University of Virginia, Charlottesville, VA 22904, USA

² Steward Observatory, University of Arizona, 933 N. Cherry Ave., Tucson, AZ 85721, USA

³ Gemini Observatory, 670 N. Aohoku Place, Hilo, HI 96720, USA

⁴ Department of Astronomy, University of California, Berkeley, CA 94720-3411, USA

⁵ Department of Astronomy & Astrophysics, University of California, San Diego, 9500 Gilman Drive, MC 0424, La Jolla, CA 92093-0424, USA

⁶ IPAC, MC 100-22, Caltech, 1200 E. California Blvd., Pasadena, CA 91125

Accepted XXX. Received YYY; in original form ZZZ

ABSTRACT

We present spectra of the supernova (SN) impostor AT 2016blu spanning over a decade. This transient exhibits quasiperiodic outbursts with a ~ 113 d period, likely triggered by periastron encounters in an eccentric binary system where the primary star is a luminous blue variable (LBV). The overall spectrum remains fairly consistent during quiescence and eruptions, with subtle changes in line-profile shapes and other details. Some narrow emission features indicate contamination from a nearby H II region in the host galaxy, NGC 4559. Broader H α profiles exhibit Lorentzian shapes with full width at half-maximum intensity (FWHM) values that vary significantly, showing no correlation with photometric outbursts or the 113 d phase. At some epochs, H α exhibits asymmetric profiles with a stronger redshifted wing, while broad and sometimes multicomponent P Cygni absorption features occasionally appear, but are again uncorrelated with brightness or phase. These P Cygni absorptions have high velocities compared to the FWHM of the H α emission line, perhaps suggesting that the absorption component is not in the LBV’s wind, but is instead associated with a companion. The lack of phase dependence in line-profile changes may point to interaction between a companion and a variable or inhomogeneous primary wind, in an orbit with only mild eccentricity. Recent photometric data indicate that AT 2016blu experienced its 20th outburst around May/June 2023, as predicted based on its period. This type of quasiperiodic LBV remains poorly understood, but its spectra and erratic light curve resemble some pre-SN outbursts like those of SN 2009ip.

Key words: stars: individual: AT 2016blu – stars: massive – stars: variables: general – galaxies: NGC 4559.

1 INTRODUCTION

AT 2016blu (also known as NGC 4559OT) is an extragalactic supernova (SN) impostor located in an outer spiral arm of its host galaxy NGC 4559, at a distance of 8.91 ± 0.3 Mpc (McQuinn et al. 2017). AT 2016blu was discovered in 2012 during the Lick Observatory Supernova Search (LOSS; Li et al. 2000; Filippenko et al. 2001; Kandrashoff et al. 2012) with the 0.76 m Katzman Automatic Imaging Telescope (KAIT). In a previous paper, we analyzed the photometric evolution of AT 2016blu (hereafter Paper I; Aghakhanloo et al. 2023b), revealing at least 19 recorded outbursts, recurring every 113 ± 2 d. Its outbursts have a typical brightness of $m_R \approx 17$ mag, corresponding to an absolute magnitude of approximately -12.8 with distance and reddening corrections. We proposed that these outbursts are caused by periastron encounters in an interacting eccentric binary system (Kashi & Soker 2010; Smith 2011), in which the primary star is a luminous blue variable (LBV).

AT 2016blu is not the only SN impostor known for its quasiperiodic outbursts. SN 2000ch in NGC 3432 experienced multiple outbursts from 2000 to 2009, as documented by Wagner et al. (2004) and Pastorello et al. (2010). Continuing this pattern, SN 2000ch has undergone a total of 23 brief outbursts since 2000 (Aghakhanloo et al. 2023a). These outbursts also repeat every 200.7 ± 2 d, which hints at a possible binary nature (Pastorello et al. 2010; Smith 2011; Smith et al. 2011; Aghakhanloo et al. 2023a), similar to AT 2016blu. In both systems, the variability of outbursts can be influenced by the intrinsic S Doradus-like variability of the primary star (van Genderen 2001; Groh et al. 2009), which may cause the binary interaction to be somewhat different at each periastron pass, with some periastron encounters leading to photometric outbursts that are weaker or even absent (Aghakhanloo et al. 2023a,b).

Both AT 2016blu and SN 2000ch have been noted for their resemblance to η Carinae. Although they are not identical to η Carinae, they exhibit similar behaviour, suggesting similar underlying physical processes. Their brief outbursts are reminiscent of the peaks observed in η Carinae in the few years leading up to its 19th century Great Erup-

* E-mail: mvy4at@virginia.edu

tion, which occurred during periastron in its binary system (Smith & Frew 2011; Smith 2011). The recurring outbursts of SN 2000ch and AT 2016blu also resemble the repeating peaks of SN 2009ip before its SN explosion (Smith et al. 2010; Pastorello et al. 2013). Notably, the LBV-like outbursts of SN 2009ip culminated in a luminous Type IIn SN-like event in 2012 (Mauerhan et al. 2013; Smith et al. 2014, 2022). This event provides compelling evidence that LBVs can be progenitors of Type IIn supernovae, contrary to most theoretical predictions (Mauerhan et al. 2013; Smith 2014). Similar LBV-like variability before an SN was also seen in SN 2015bh (Elias-Rosa et al. 2016; Boian & Groh 2018).

Given the similarities in photometric evolution between AT 2016blu, SN 2000ch, and other well-known LBVs such as η Carinae and SN 2009ip, it is pertinent to study their spectral evolution as well. LBVs, being highly variable stars, exhibit significant spectral changes over time. Traditional expectations are that during outbursts, they resemble cool supergiants with spectral types A or F, and during the quiescent state, they appear as hotter B-type supergiants or Of/WN stars (see Smith 2017, for a review). LBVs in cool outburst states typically exhibit a temperature around 8000 K, and display a combination of absorption, emission, and P Cygni lines, with line widths suggesting relatively slow outflow speeds between 100 and 500 km s⁻¹. This is not always true, however, as a subset of LBVs has been shown to brighten at relatively constant (hot) temperatures (Smith et al. 2020, 2011). This class of hot LBV outbursts includes the precursor of SN 2009ip (Smith et al. 2010), SN 2000ch (Wagner et al. 2004; Smith et al. 2011), HD 5980 (Koenigsberger 2004), and both MCA-1B (Smith et al. 2020) and Romano’s star (Polcaro et al. 2016) in M33. SN 2009ip, for instance, exhibited strong, narrow emission lines with a speed of about 550 km s⁻¹ during its pre-SN outbursts, similar to that observed in other SN impostors (Van Dyk 2007; Smith et al. 2011; Van Dyk & Matheson 2012), but it maintained a blue continuum slope and He I emission lines at all phases (Smith et al. 2010). Some lines in SN 2009ip also showed weak, broad, and blueshifted absorption wings reaching high velocities up to $\sim 10,000$ km s⁻¹ (Smith et al. 2010; Pastorello et al. 2013). Similarly, η Carinae primarily shows eruptive outflows at speeds around 600 km s⁻¹ or less, but about 1% of its material reaches much higher speeds of 5000 to 10,000 km s⁻¹ (Smith 2008; Smith et al. 2018a,b).

Wagner et al. (2004), Pastorello et al. (2010), and Smith et al. (2011) also studied the optical spectra of SN 2000ch, revealing evolving spectral characteristics. Wagner et al. (2004) observed changes in Balmer emission lines and the absence of typical LBV spectral features like Fe II lines, consistent with maintaining a hotter temperature in outburst, as noted above. Pastorello et al. (2010) reported significant changes in spectral features, including increased H α width, stronger He I lines, and the emergence of P Cygni profiles. These observations also showed some exceptionally high terminal wind velocities, unusual for known LBV winds. Overall, SN 2000ch’s spectral features varied, but resembled those of some SN impostors like SN 2009ip and H-rich Wolf–Rayet (WR) stars.

In this paper, we analyze the spectroscopic evolution of AT 2016blu and explore its similarities with other SN impostors. Section 2 presents the latest photometric and spectroscopic observations. In Section 3, we document the new outbursts observed since the publication of Paper I until 2024. Section 4 discusses the spectral evolution of various lines, and Section 5 covers the H α emission-line profiles, including the estimation of full width at half-maximum intensity (FWHM) values. Section 6 focuses on comparing the spectra of AT 2016blu with those of SN 2000ch and SN 2009ip. We discuss our findings in Section 7, and conclude with a summary in Section 8.

2 OBSERVATIONS

2.1 New Photometry

Paper I presents the optical and infrared photometry of AT 2016blu from 1999 to 2022. This work includes updated optical photometry of AT 2016blu using the latest data from multiple sources: the *Gaia* space telescope (Gaia Collaboration et al. 2016), the Zwicky Transient Facility (ZTF; Bellm et al. 2019) public survey, and the ATLAS Project (Asteroid Terrestrial-impact Last Alert System; Tonry et al. 2018). For detailed information about photometry, refer to Paper I. Fig. 1 shows the updated light curve, and Fig. 2 displays the zoomed-in light curves for the recent outbursts (see Section 3 for more details).

2.2 Spectroscopy

We obtained optical spectra of AT 2016blu using the BlueChannel and Binospec (Fabricant et al. 2019) Spectrographs on the 6.5 m Multiple Mirror Telescope (MMT). Observations with the MMT BlueChannel were performed using 1200 and 300 lines mm⁻¹ gratings, with approximate resolutions of 1.5 and 6.5 Å (roughly 70 and 300 km s⁻¹). Meanwhile, the MMT Binospec observations utilised a 1000 lines mm⁻¹ grating with a nominal spectral resolution $R = \lambda/\Delta\lambda$ of about 3900 (~ 80 km s⁻¹), although some of our spectra had somewhat better resolution on nights with good seeing. Reductions for the MMT BlueChannel were carried out using IRAF¹. Flux calibration was achieved using spectrophotometric standards at similar airmasses, taken during the same night as the observation. The MMT Binospec data were reduced using the Binospec pipeline (Kansky et al. 2019). All MMT spectra are plotted in Figs. 3a, 3b, and 4a.

Two spectra were obtained at the W. M. Keck Observatory using the Deep Imaging Multi-Object Spectrograph (DEIMOS; Faber et al. 2003) with $R \approx 4400$ (~ 70 km s⁻¹), and one spectrum was collected at Keck using the Low-Resolution Imaging Spectrometer (LRIS; Oke et al. 1995), with $R \approx 1000$ (~ 300 km s⁻¹). Additionally, spectra were acquired using the Kast double spectrograph on the Lick 3 m Shane reflector with $R \approx 700$ (~ 430 km s⁻¹). These Keck and Lick spectra were reduced using standard techniques, including bias subtraction, flat-fielding, local sky subtraction, and extraction of one-dimensional spectra. Fig. 4b presents all the spectra from the Keck and Lick Observatories.

The DEIMOS spectrum from 2013-02-17 and MMT BlueChannel spectra from 2012-01-31 and 2012-04-17 exhibit narrow absorption features superimposed on emission lines. These are likely due to oversubtraction of the background sky and surrounding H II region emission during data reduction; they are thus artifacts, as similar features are not observed at any other time.

Optical spectra were also obtained using the Boller & Chivens (B&C) spectrograph on the 2.3 m Bok telescope, utilising both 1200 and 300 lines mm⁻¹ gratings with approximate resolutions of 1.8 and 8 Å (~ 80 and 370 km s⁻¹), respectively. Data reduction for these spectra was performed following standard IRAF procedures. The Bok spectra are displayed in Figs. 5a, and 5b.

All reduced spectra have been corrected for the redshift of

¹ IRAF is distributed by the National Optical Astronomy Observatory, which is operated by the Association of Universities for Research in Astronomy (AURA) under a cooperative agreement with the U.S. National Science Foundation.

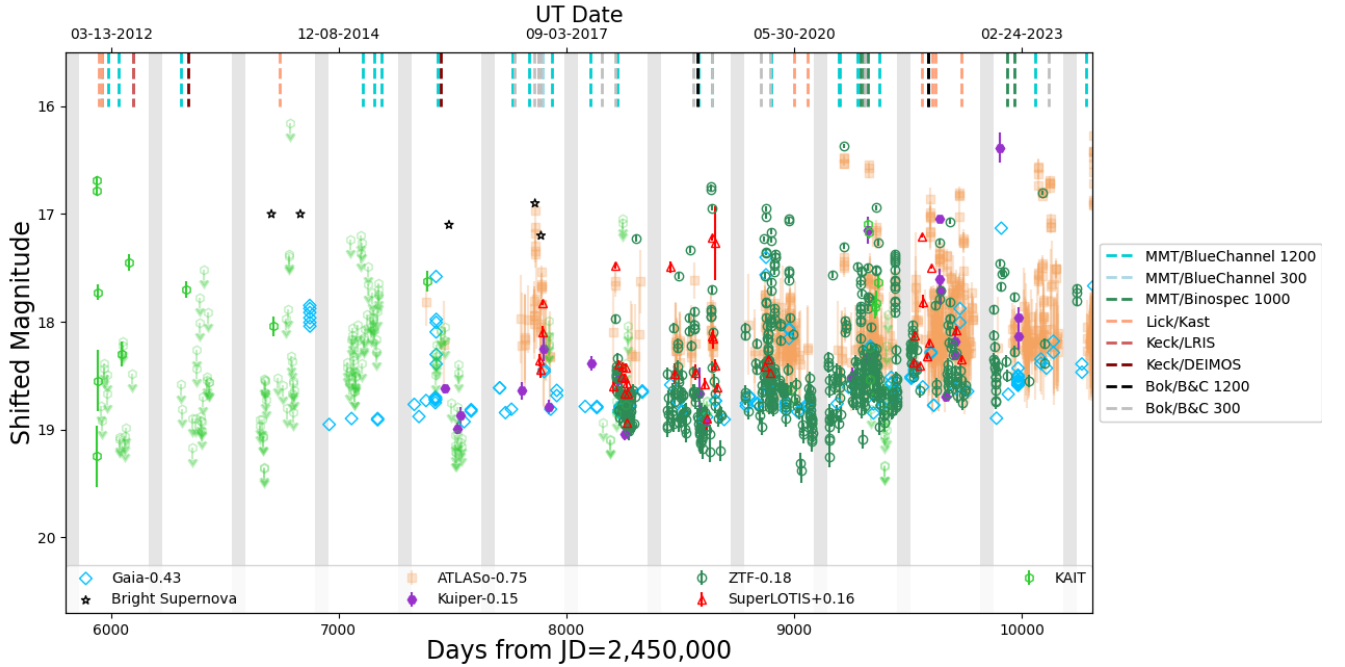


Figure 1. The updated photometric evolution of AT 2016blu until January 2024. Epochs of spectroscopic observations are marked with vertical ticks. Grey vertical sections highlight periods each year, from August 26 to October 24, when observing AT 2016blu is challenging owing to its proximity to the Sun in the sky. For a closer look at recent outbursts, see Fig. 2.

AT 2016blu’s host, which is $z = 0.00261$. The UTC dates of observation are listed next to each spectrum.

3 UPDATED LIGHT CURVE

Fig. 1 shows the most updated light curve for AT 2016blu from 2012 until 2024. The solid vertical grey bands mark the time interval each year, from August 26 to October 24, during which AT 2016blu is challenging or impossible to observe due to its proximity to the Sun in the sky. All the spectroscopic data are marked with dashed vertical lines in the light curve. Photometric data from ZTF are in the r band, *Gaia* in the G band, and ATLAS in the o band. Therefore, we have adjusted the fluxes from each dataset to approximately match the base quiescent magnitudes across all datasets. Recent photometric observations reveal that AT 2016blu experienced another peak in March 2022. This peak was not covered in the data available at the time of the first paper’s publication. Additionally, we have observed that AT 2016blu experienced an outburst in 2023 as predicted in Paper I. Fig. 2 shows a zoomed-in version of the light curve for each event.

In this section, we provide a detailed description of each event. The designation for each event corresponds to the date of the two brightest peaks. According to Paper I, the outbursts appear to recur with a likely periodicity of ~ 113 d. As explained in Paper I, the bright eruption events are very brief (a few days or weeks), and instead of one eruption landing at the expected time for the periodicity (given by the red vertical line in Fig. 2), we see groups of several brightening events clustered around the predicted period. According to the scenario outlined in Paper I, this may arise from a companion interacting with a clumpy wind or series of shells ejected irregularly

by the LBV, with a tendency to occur more often near periastron, but not exactly at the time of periastron. Additionally, a lower amplitude peak was found roughly at 39 d, which is probably related to multiple spikes occurring either before or after each outburst (see Paper I). Each plot features a red dashed line indicating the expected time of the outburst, which is derived from $d_{\text{red}} = 2,455,938.9 + 113 n$. A brown dotted line in each plot marks the reference epoch, determined using the second most dominant period found in the periodogram.

March/April 2022: In Paper I, we documented the 18th outburst of AT 2016blu. The peak observed was more consistent with the shorter period, as indicated by a brown dotted line, rather than the longer period marked by a red dashed line. New data from ZTF DR20 suggest that, similar to many of AT 2016blu’s previously documented outbursts, this event also exhibited multiple peaks of approximately similar magnitudes; see Fig. 2a for details.

May/June 2023: Based on the detected period of approximately 113 d, it was predicted that AT 2016blu would experience an outburst in late June 2023. Fig. 2b shows that AT 2016blu underwent its 20th recorded outburst, reaching an apparent magnitude of 16.8 in May 2023. ATLAS data suggest that AT 2016blu had another peak in June, which aligns more closely with the predicted time of the outburst. Dedov et al. (2023) also monitored AT 2016blu around the proposed time and reported an outburst of AT 2016blu in late June, reinforcing the ATLAS data.

4 OVERVIEW OF THE SPECTRA

The spectra of AT 2016blu are shown in Figs. 3–5. Each spectrum is labeled with the UTC date of observation, the number of days relative to a documented peak in the light curve, the orbital phase

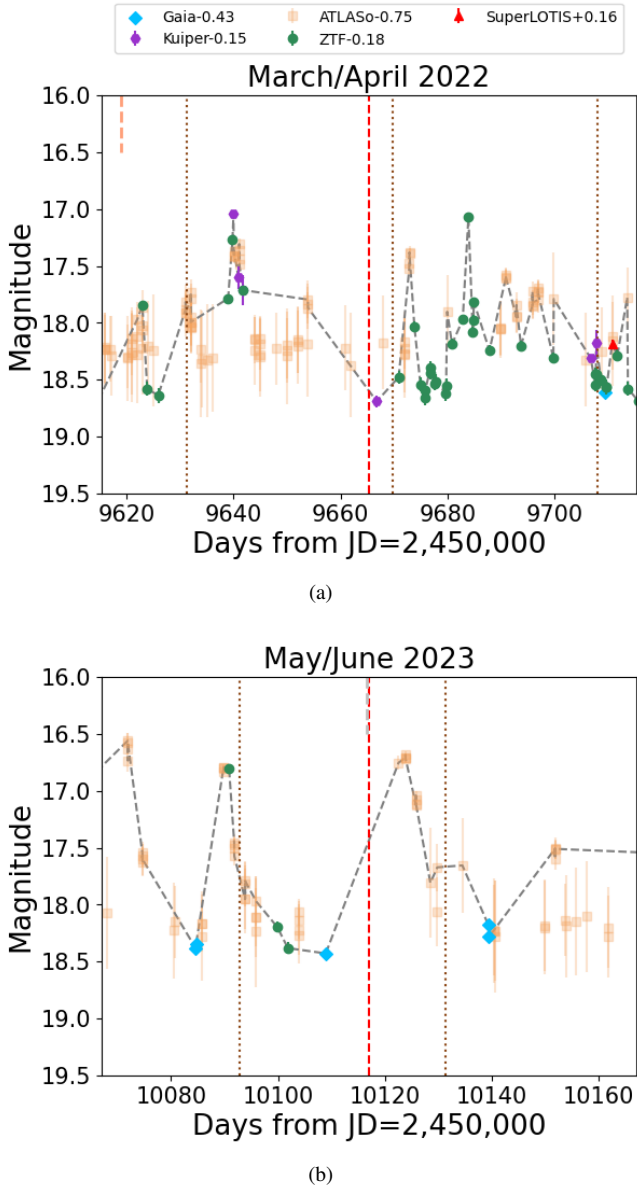


Figure 2. Zoomed-in views of the light curve of AT 2016blu during its recent outbursts, with the timing of each event indicated at the top of the frame. The red dashed line marks the reference epoch, based on the most probable period of about 113 d, linked to the first January 2012 outburst. The brown dotted line represents the reference epoch using the second significant peak identified in the period analysis, around 38.5 d (Aghakhanloo et al. 2023b).

using a period of 113 d, and interpolated magnitudes at the time the spectrum was observed. We estimated the system’s approximate R magnitude at the time of the spectroscopic observations using all available photometry, excluding faint ATLAS data, which are noisy due to AT 2016blu’s brightness being comparable to the telescope’s limiting magnitude. Spectra with “nan” magnitudes indicate that no magnitude could be interpolated owing to the absence of photometric data within 30 days of the spectroscopic observation. Given the brief and erratic nature of AT 2016blu’s outbursts, any future data releases, which may include older, previously unreleased photometry, could lead to updated magnitudes. Spectra that have an interpolated magnitude brighter than 18 and are captured within 15 days of peak brightness in the light curve are highlighted in yellow, while those

taken during quiescent states are shaded grey. For spectra not highlighted, insufficient photometry makes it difficult to determine the state of the system at the time of the spectroscopic observation. All spectra are scaled using the continuum portion of each spectrum.

AT 2016blu’s spectra are dominated by strong hydrogen Balmer emission lines with narrow peaks and broadened wings. Various lines are identified across all spectra. However, not all lines are visible in every epoch. Notably, a handful of spectra (e.g., MMT/BlueChannel 1200) show weak Fe II lines, but the majority of the spectra lack the Fe II and [Fe II] emission lines that are commonly observed in the spectra of LBVs (Hillier et al. 2006; Mehner et al. 2017). Some spectra also show Ca II, and O I lines. However, the absence of strong Fe II and Ca II in most spectra and the presence of He I emission lines suggests that AT 2016blu is significantly hotter than a typical LBV in its eruptive state, as noted above. While P Cygni profiles are occasionally evident, some spectra do not display the characteristic P Cygni profiles typical of LBVs in outburst. Despite some subtle changes in details, such as the width of $H\alpha$ and the variable P Cygni absorption, the overall optical spectrum of AT 2016blu remains fairly consistent throughout both the outburst and quiescent states.

[S II] and strong [O III] lines have also been detected, suggesting potential contamination from a neighbouring H II region. This is supported by a narrow component observed overlaying the broader $H\alpha$ emission base, as shown in Figs. 4a and 5b, although some of the narrow $H\alpha$ could also originate from circumstellar material (CSM). It remains challenging to determine the extent of contribution from the H II region where AT 2016blu is located. The Binospec pipeline selects a local sky position, while the BlueChannel data are reduced by subtracting the H II region emission, leading to variations in the strength of the narrow lines originating from the H II region. Notably, during several MMT/BlueChannel epochs where the H II region emissions have been effectively subtracted, we do not detect significant narrow $H\alpha$ emission in the transient. This strongly suggests that the observed narrow components primarily originate from the H II region, and thus have been excluded from our FWHM analysis (see Section 5).

4.1 Hydrogen Balmer Lines

Figs. 6 and 7 show a subset of spectra around the $H\alpha$ profile, focusing on the velocity range of $\pm 6500 \text{ km s}^{-1}$. As previously mentioned, the $H\alpha$ profile features a narrow component superimposed on a broad component, likely due to contamination from nearby H II regions or CSM. These narrow components are clearly visible in high-resolution spectra, but remain unresolved in other low and mid-resolution spectra.

In some spectra, such as those from 2016-02-16 and 2017-03-22 in the BlueChannel 1200 grating, the $H\alpha$ profile is broader and asymmetric, exhibiting a hump on the red side, or a deficit on the blue wing. In other spectra, the broad component of $H\alpha$ has a redshifted centroid, while the narrow component of the emission profile remains centred close to the $H\alpha$ rest wavelength. In Section 5, we discuss radial-velocity variations across the orbital period.

Figs. 6 and 7 also show that $H\alpha$ exhibits P Cygni profiles at some epochs, which are typical during the outburst state of LBVs (Mehner et al. 2017). However, P Cygni features are also observed during the quiescent state, and in some instances of outburst states of AT 2016blu no P Cygni features are detected. The $H\alpha$ profile also displays a Lorentzian shape, and the FWHM of the $H\alpha$ profile varies over time. Detailed analyses and discussions regarding the FWHM measurements of the $H\alpha$ lines are presented in Section 5.

Figs. 3b, 4b, and 5a also show higher-order Balmer emission lines.

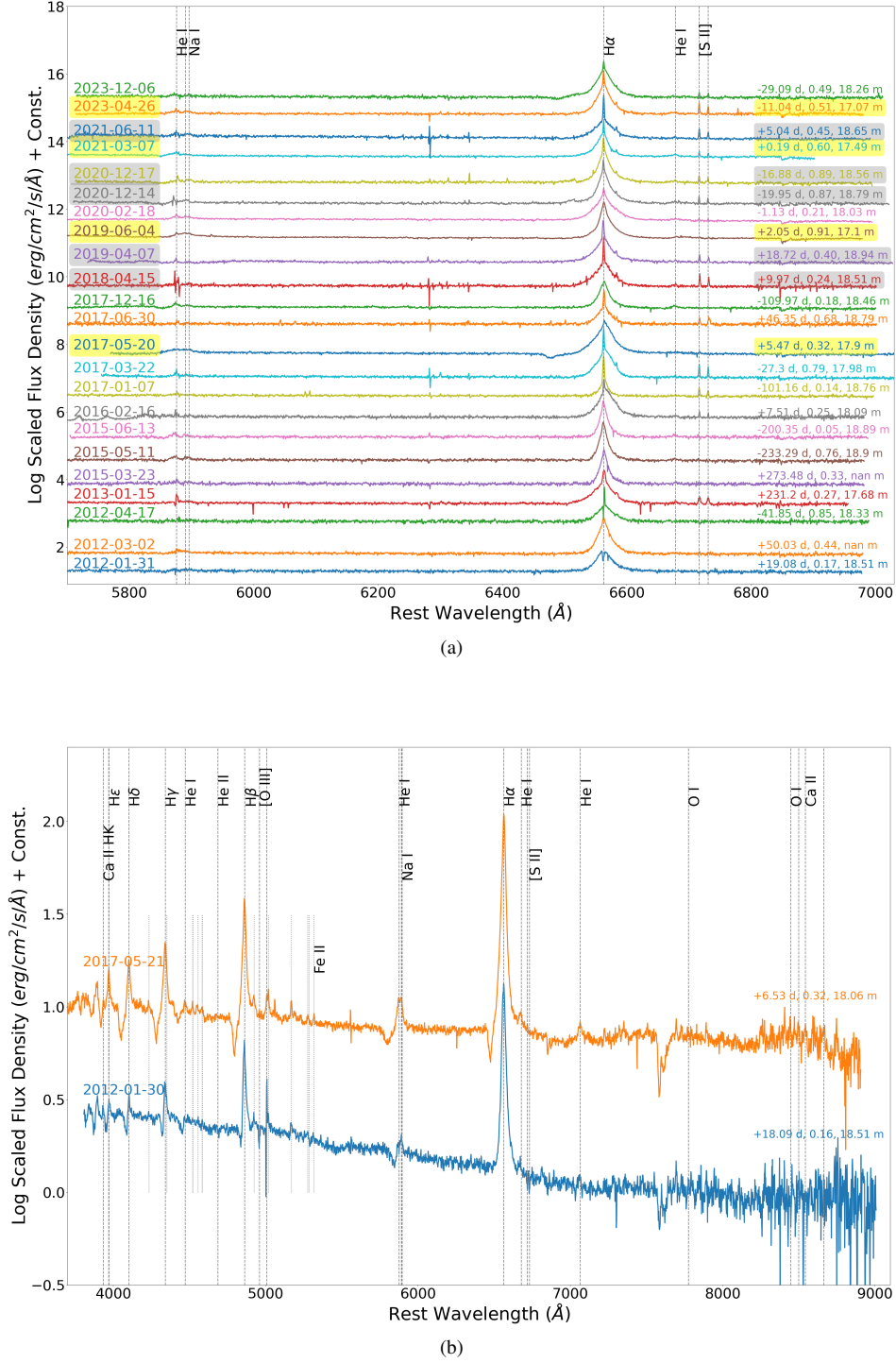


Figure 3. Optical spectra of AT 2016blu obtained with MMT/BlueChannel using gratings with 1200 lines mm^{-1} (top panel) and 300 lines mm^{-1} (bottom panel). Note that all spectra throughout the paper have been corrected for the adopted host-galaxy redshift of $z = 0.00261$. Spectra corresponding to times when AT 2016blu had an interpolated magnitude brighter than 18 and are taken within 15 days of peak brightness are annotated in yellow. Spectra most likely taken during the quiescent state are annotated in grey. The three values on the right side show the days after or before the documented peak brightness, the 113 d period phase, and the interpolated magnitude at the time the spectrum was taken. Balmer, He I, and Fe II lines, as well as P Cygni profiles, are visible.

Since using a higher spectral resolution grating reduces the spectral range, the higher-order Balmer lines are only visible in low-resolution spectra. P Cygni absorption components are also distinctly visible in some of the higher-order Balmer lines. Absorption features are generally stronger compared to those in H α (see Fig. 8). Similar to the

spectra obtained on May 13, 2021, and March 15, 2021, by [Valeev et al. \(2021\)](#) and [Vinokurov et al. \(2021\)](#), some of our observations reveal double-dip absorption features in higher-order Balmer lines, characterised by two distinct minima within the absorption profile (e.g., 2022-01-27 and 2022-02-08, Lick spectra). The double-dip ab-

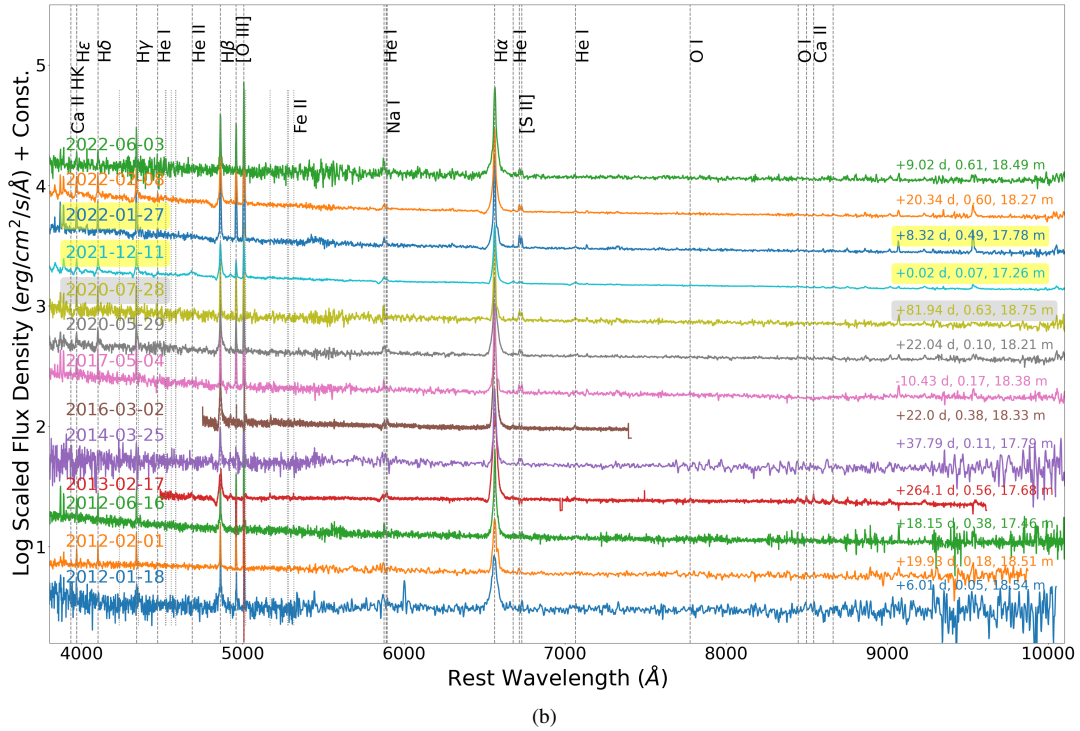
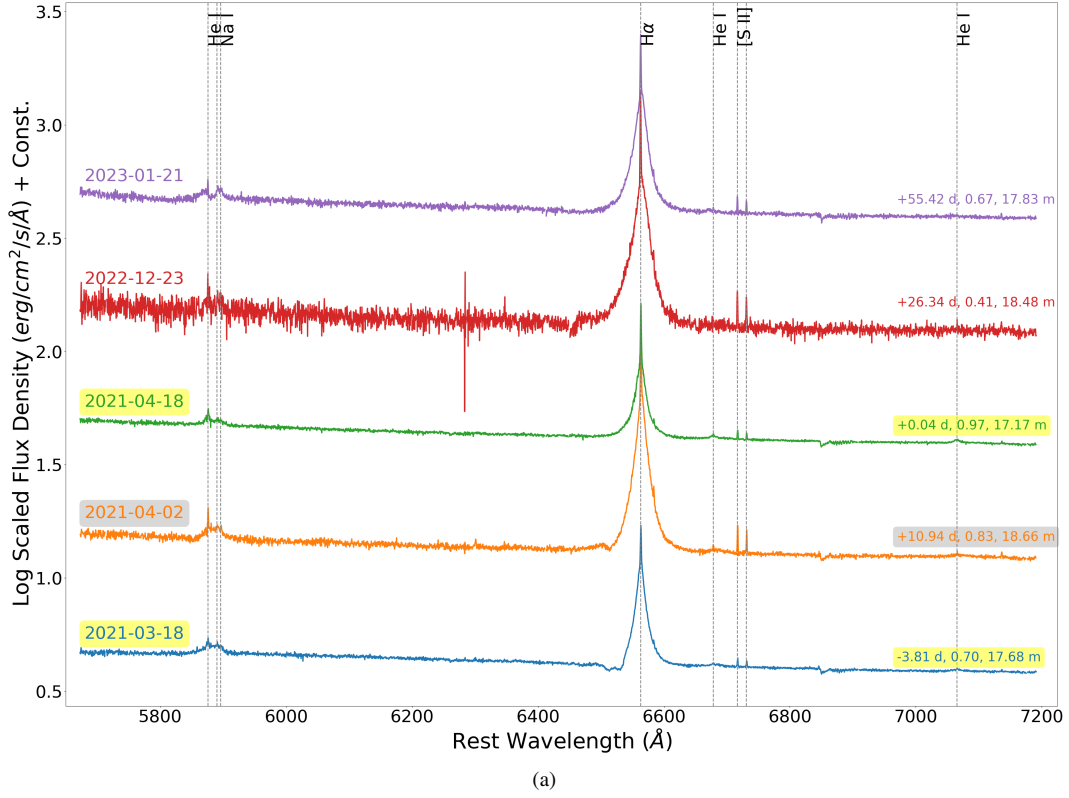


Figure 4. The top panel shows the spectra of AT 2016blu from MMT/Binospec. The Binospec data reveal narrow H α emission from the underlying H II region or CSM. Binospec spectra also display He I lines during both outburst and quiescent states. The bottom panel shows a series of high-, moderate- and low-resolution spectra of AT 2016blu from Keck/LRIS, Keck/DEIMOS, and Lick/Kast. Some spectra show O I and Ca II lines.

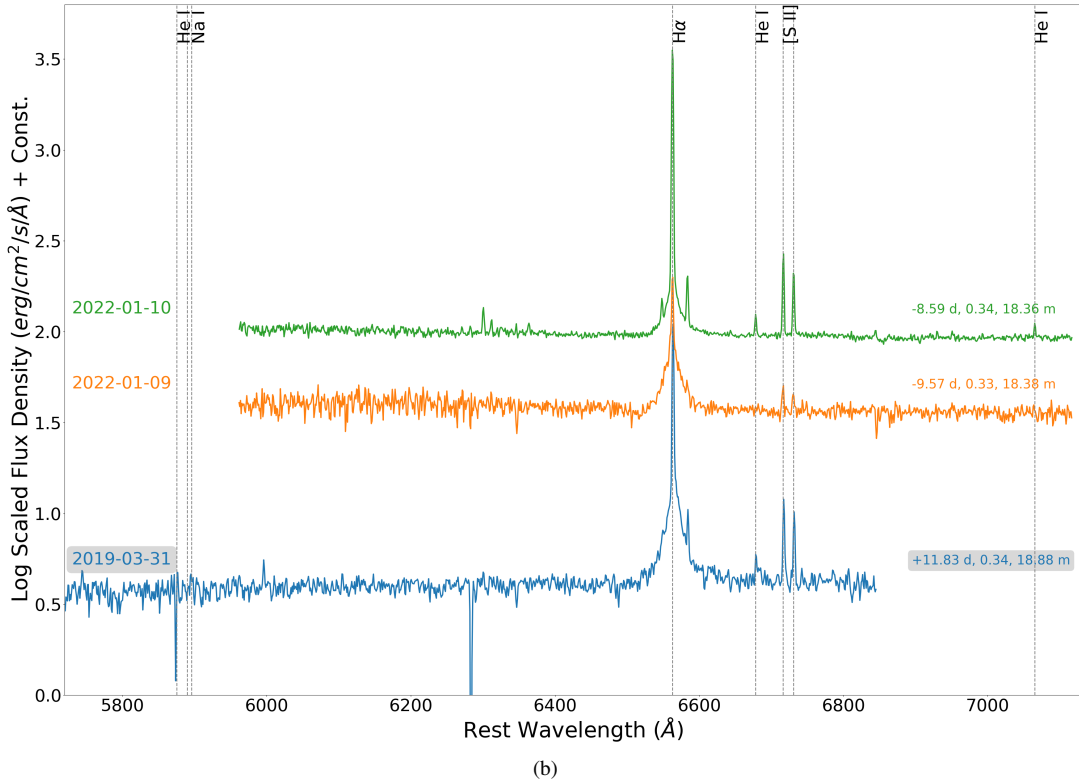
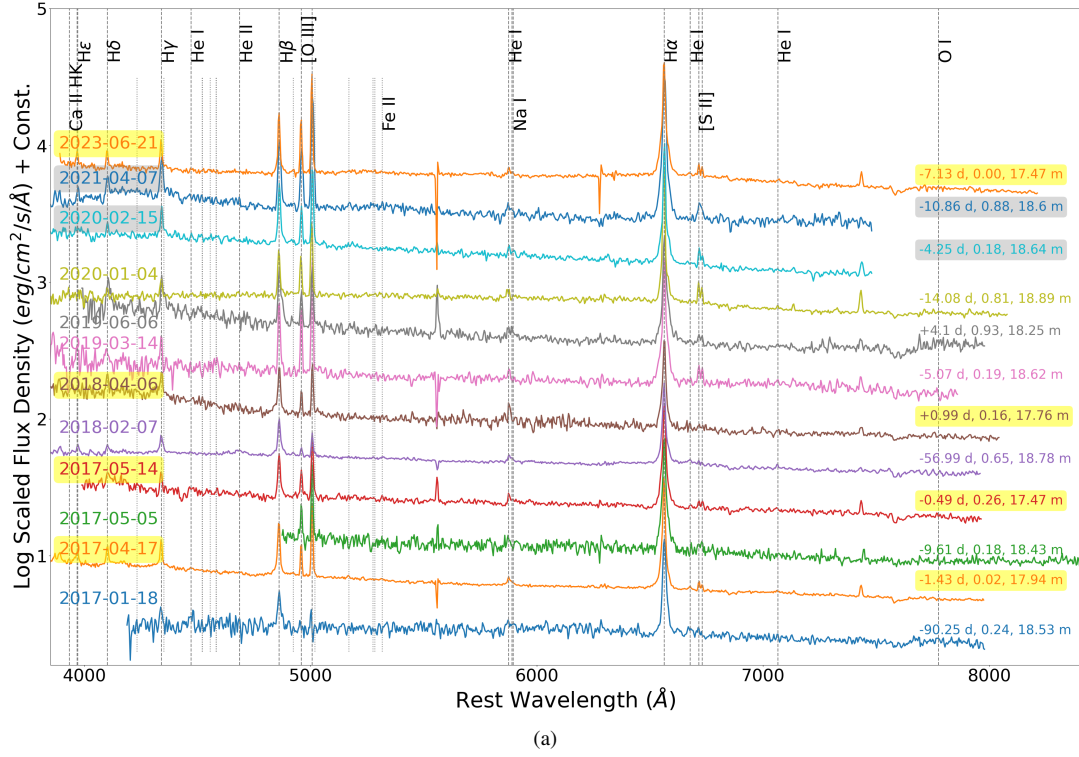


Figure 5. Optical spectra of AT 2016blu from Bok B&C. The top and bottom panels show the 300 and 1200 lines mm^{-1} gratings, respectively. Similar to the Binospec spectra, contamination from a nearby H II region is evident in the bottom panel.

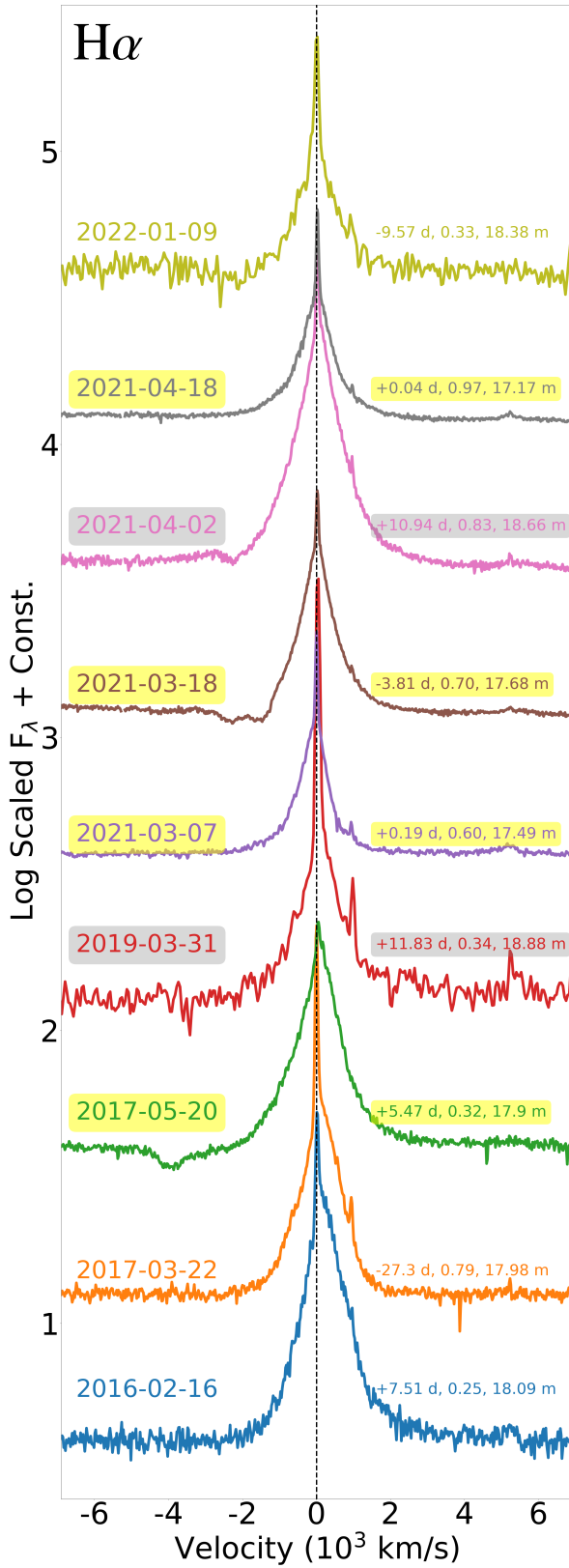


Figure 6. Velocity profile of a subset of H α from high-resolution spectra. P Cygni features are detected in both outburst and quiescent states. The 2021-03-18 spectrum also shows a double-dip absorption feature, and some spectra, such as those from 2017-03-22, exhibit a red hump.

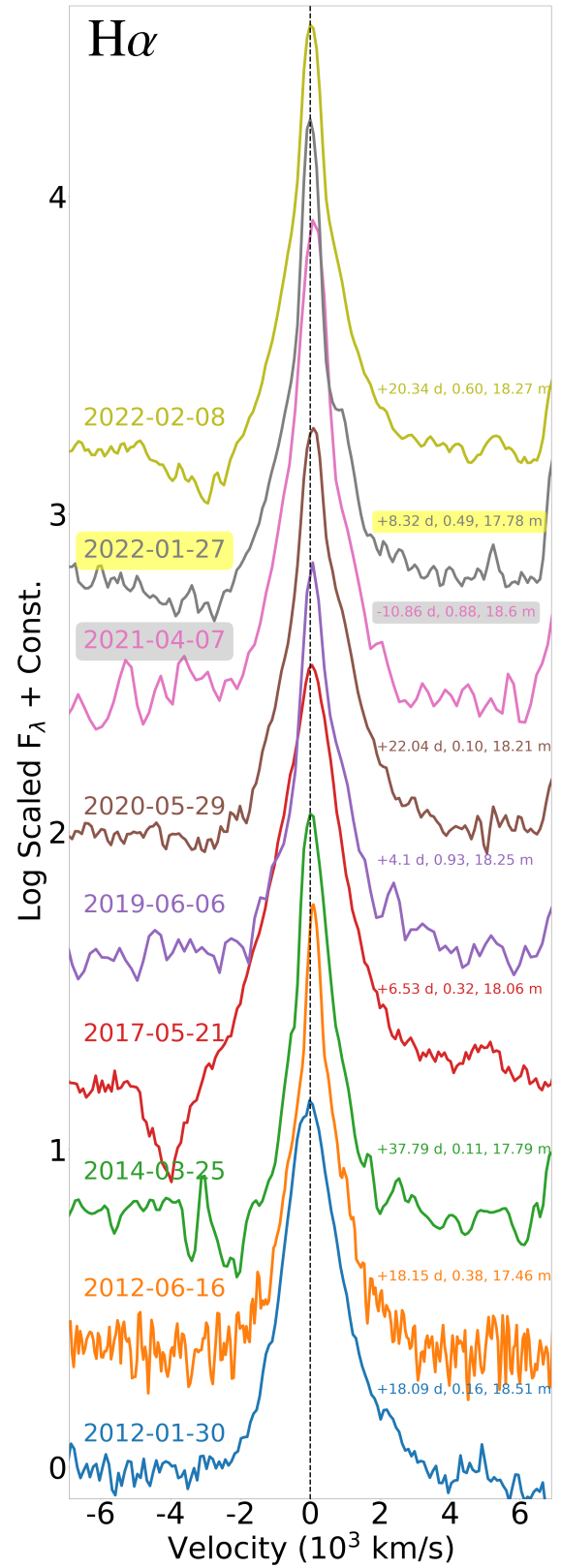


Figure 7. Same as Fig. 6, but low-resolution data. Double-dip absorption features are visible in some spectra such as those from 2014-03-25 and 2022-01-27.

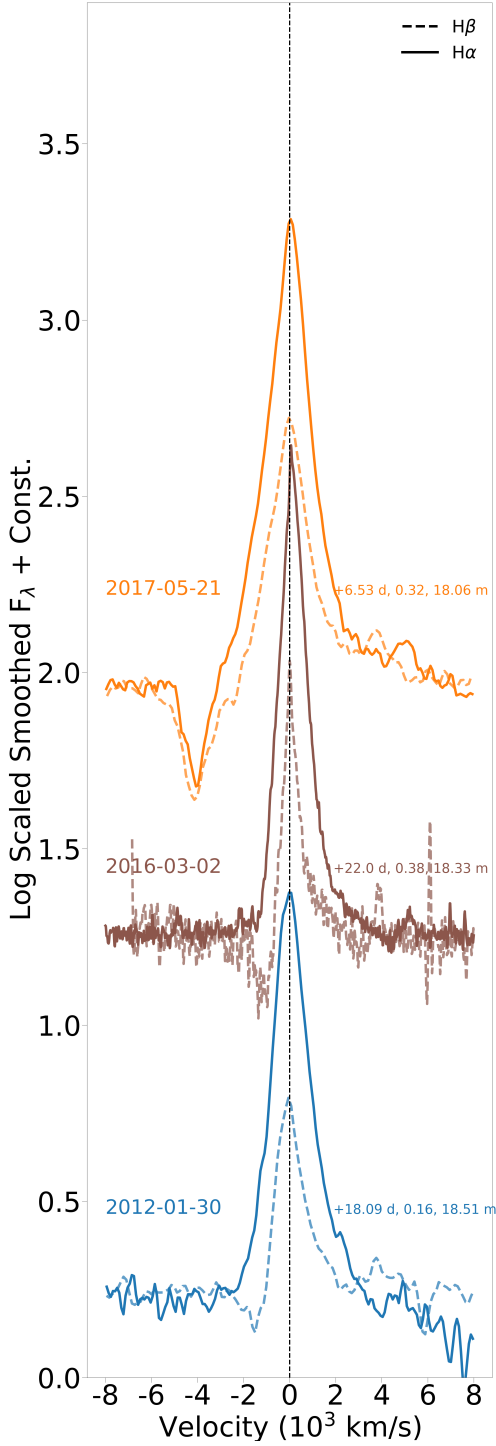


Figure 8. Velocity profiles of the $H\alpha$ and $H\beta$ lines. Absorption features are generally stronger in the higher-order Balmer lines, and the P Cygni absorption occurs at a wide range of different velocities.

sorption feature is also visible in the $H\alpha$ line in the high-resolution Binospec spectra taken on March 18, 2021 (see Fig. 6), as well as in some of the Lick spectra (see Fig. 7). The Binospec spectrum was obtained 4 days before a luminosity peak in the light curve. Interestingly, a subsequent Binospec spectrum, taken 15 days later, reveals that the double dips have merged into a single absorption feature, and later, on April 18, 2021, the P Cygni absorption disappears

completely. There is a possibility that some double-dip features were missed owing to the low resolution of some of the spectra. Vinokurov et al. (2022) also reported no detection of any distinct double-dip absorption features in $H\beta$ and $H\gamma$. P Cygni absorption features with multiple or discrete components are sometimes seen in the variable winds of LBVs (Richardson et al. 2011; Stahl et al. 2003, 2001; Leitherer et al. 1994; Stahl et al. 1983), and these have been linked to wind variability resulting from the bistability jump (Groh & Vink 2011). However, we note that the velocities seen here in AT 2016blu are significantly faster than the typical speeds of $100\text{--}200\text{ km s}^{-1}$ when these are seen in normal LBVs.

4.2 He I Lines

Figs. 9 and 10 show various He I velocity profiles, with all spectra smoothed. Fig. 9a shows Binospec spectra, revealing strong He I features in both outburst and quiescent states, except on 2022-12-23 when the spectrum is significantly noisy. The high resolution of the instrument allows for the identification of both a narrow component around the He I rest velocity and a broad component. Since bright Na I emission is not expected in H II regions, the narrow component in this case might be attributed to CSM emission. Additionally, Fig. 9b shows spectra from the BlueChannel 1200 grating. On dates such as 2019-06-04 and 2017-05-20, the spectra exhibit strong He I features during the outburst state, while on other dates like 2012-04-17, the He I feature appears very weak or nearly absent.

Figs. 10a and 10b show the He I velocity profiles from BlueChannel 300 spectra, along with selected spectra from Lick and Keck data. The B&C 300 He I velocity profiles are not shown owing to low resolution; however, Fig. 5a indicates that weak He I features are also detected in B&C 300 spectra. In Fig. 10, $H\beta$ is shown as a solid line. The He I + Na I feature is centred using the He I rest wavelength (dotted line) and Na I rest wavelength at 5889.95 \AA (dashed line). The alignment of the He I + Na I feature appears consistent with the He I rest wavelength. Most likely, the absorption features are associated with He I, while the emission features are a combination of He I and Na I. Fig. 10a, and 10b also reveal that both the $H\beta$ and He I + Na I features display P Cygni profiles simultaneously.

5 $H\alpha$ PROFILE FIT

Fig. 11 shows that the $H\alpha$ emission lines have a Lorentzian profile rather than a Gaussian profile. This broadening could be a result of electron scattering or the presence of moving material, or both, though not moving at velocities comparable to those of SN ejecta. To estimate the FWHM of the $H\alpha$ lines, we combine a Lorentzian function, representing the spectral line, with a constant background to account for the underlying continuum. Fig. 11 shows examples of Lorentzian fits applied to selected spectra.

To fit the broader emission features and minimise the influence of the narrow emission peak at the centre of the $H\alpha$ profile, we exclude the data points in close proximity to the $H\alpha$ narrow peak – specifically, within $\pm 160\text{ km s}^{-1}$ – for MMT/BlueChannel 1200 grating and MMT/Binospec spectra. For spectra with lower resolution, we exclude a larger range around the peak to account for the unresolved narrow component. The extent of the area excluded varies with the resolution of the instrument, which affects the estimated FWHM of $H\alpha$, making it either narrower or broader. Given that some of the $H\alpha$ profiles are asymmetric with a red hump, we mirrored the red wing of the line profile over to the blue side to create a symmetric profile.

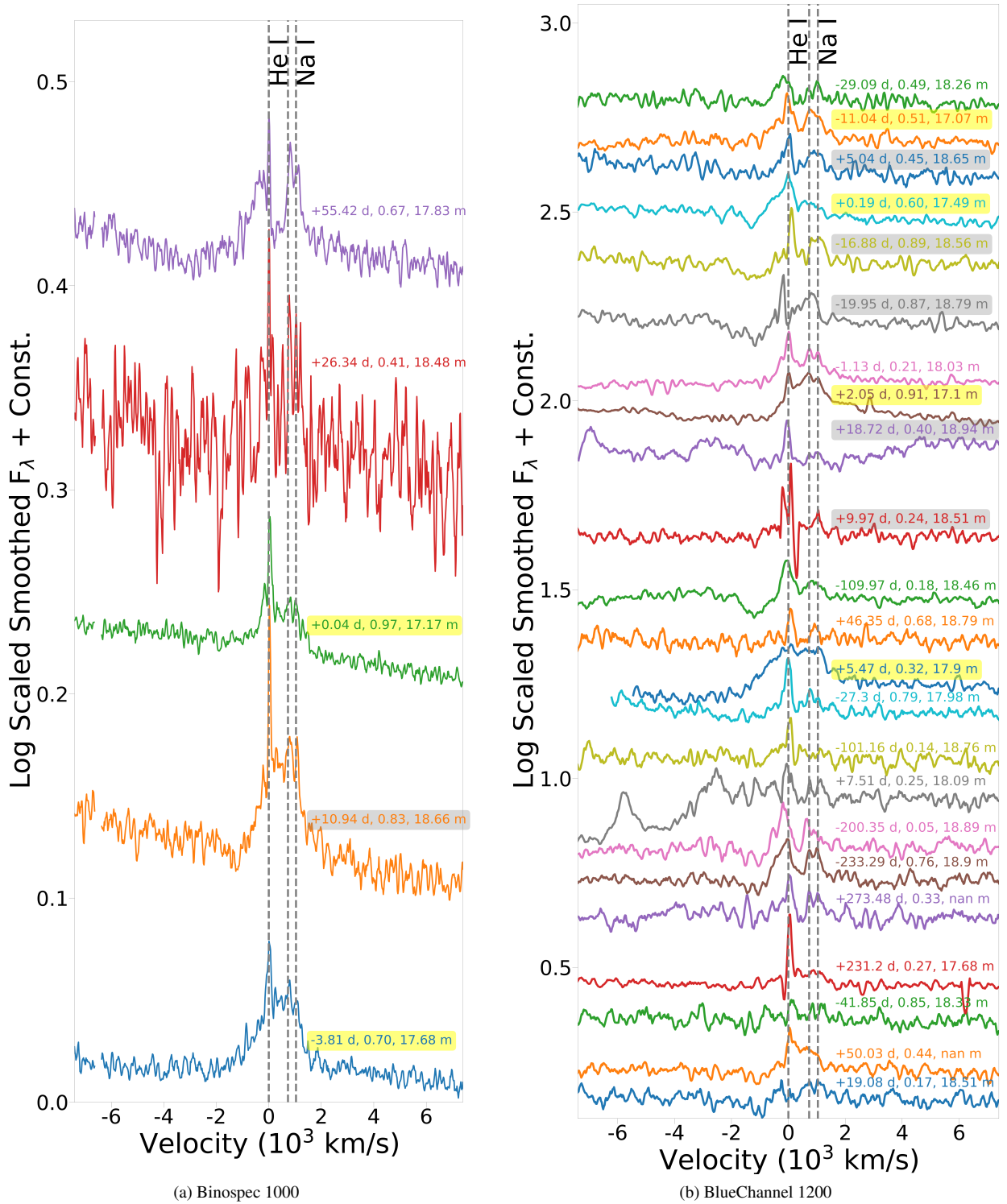


Figure 9. Spectral evolution of the He I line profile observed with the Binospec and BlueChannel instruments. The spectra are smoothed. Over time, the strength and shape of the He I line change, displaying variations such as P Cygni profiles, and at times appearing very strong or nearly absent. The left panel shows narrow components on top of broad components due to CSM emission.

This method was consistently applied to all spectra to maintain uniformity in our FWHM analysis. Consequently, the estimated FWHM can be larger if the red side is stronger (see Figs. 11a, 11b, and 11c) or smaller if the red side is weaker (see Figs. 11d). The Lorentzian

fits, shown by dotted points in the figures, are confined to the velocity range of -5000 to 5000 km s^{-1} .

We use the curve-fit function from the SciPy library in Python to perform the fits. The FWHM of the Lorentzian components was determined from the width parameter derived from these fits. Vertical

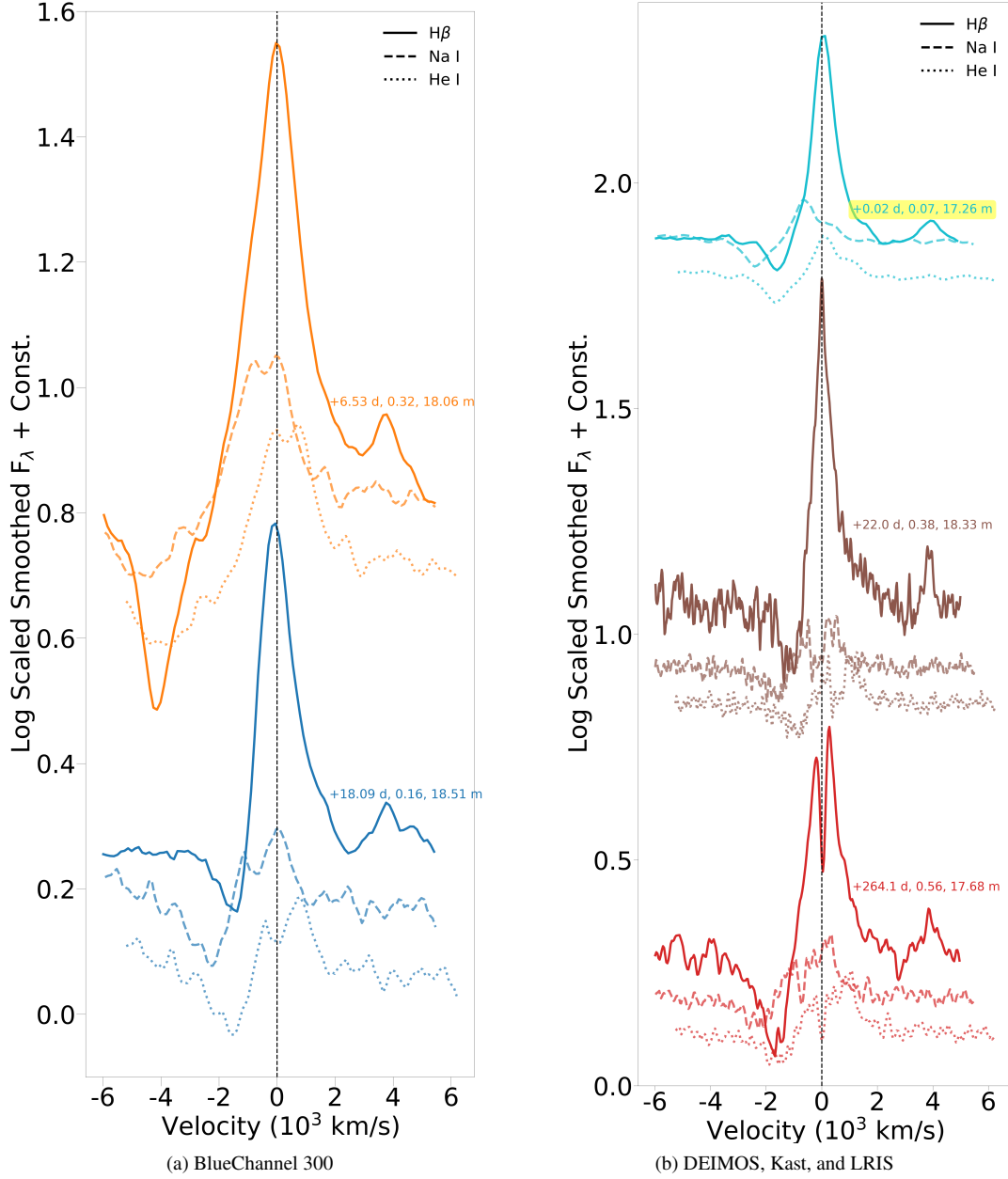


Figure 10. Velocity profiles of the H β and He I + Na I lines. The solid line represents the H β profile, while the He I + Na I blend is shown with non-solid lines: dotted lines indicate features centred at the He I rest frame, and dashed lines at the Na I rest frame. The P Cygni absorption feature aligns more closely with H β when centred at the He I rest velocity rather than at the Na I rest velocity.

dashed lines in the figures mark the FWHM of the Lorentzian peaks. The uncertainty in the FWHM was estimated by taking the square root of the diagonal elements of the covariance matrix associated with the fit width, with an additional term for residual variance to account for model-data deviations. The uncertainty in the FWHM is visually represented by shaded bars around these dashed lines, indicating potential variability due to fitting errors. Furthermore, uncertainties in the parameters of the Lorentzian fit, particularly the width, are illustrated by shaded regions around the main fit lines, which are estimated by adjusting the width parameter by \pm the uncertainty of the width. It is important to note that FWHM uncertainties do not account for uncertainties due to instrument resolution, meaning that FWHM estimates for lower-resolution spectra are much more

uncertain than those for high-resolution ones. The calculated FWHM values and their uncertainties are summarised in Table A1.

Fig. 12 shows the estimated FWHM of only high-resolution spectra. The FWHM values have been corrected for instrumental resolution and are plotted against the interpolated magnitudes at the time the spectra were obtained (left panel), and the ~ 113 d period phase cycle (right panel). No clear correlation is observed between the FWHM values and either the eruptive or quiescent states, or with the phase. Instrument resolutions are listed in Section 2.2. Spectra with interpolated magnitudes brighter than 18, obtained within 15 days of a documented peak in the light curve, are plotted with filled dark shade symbols. Spectra taken during quiescent states are shown with lighter shade filled symbols. Corrected FWHM values

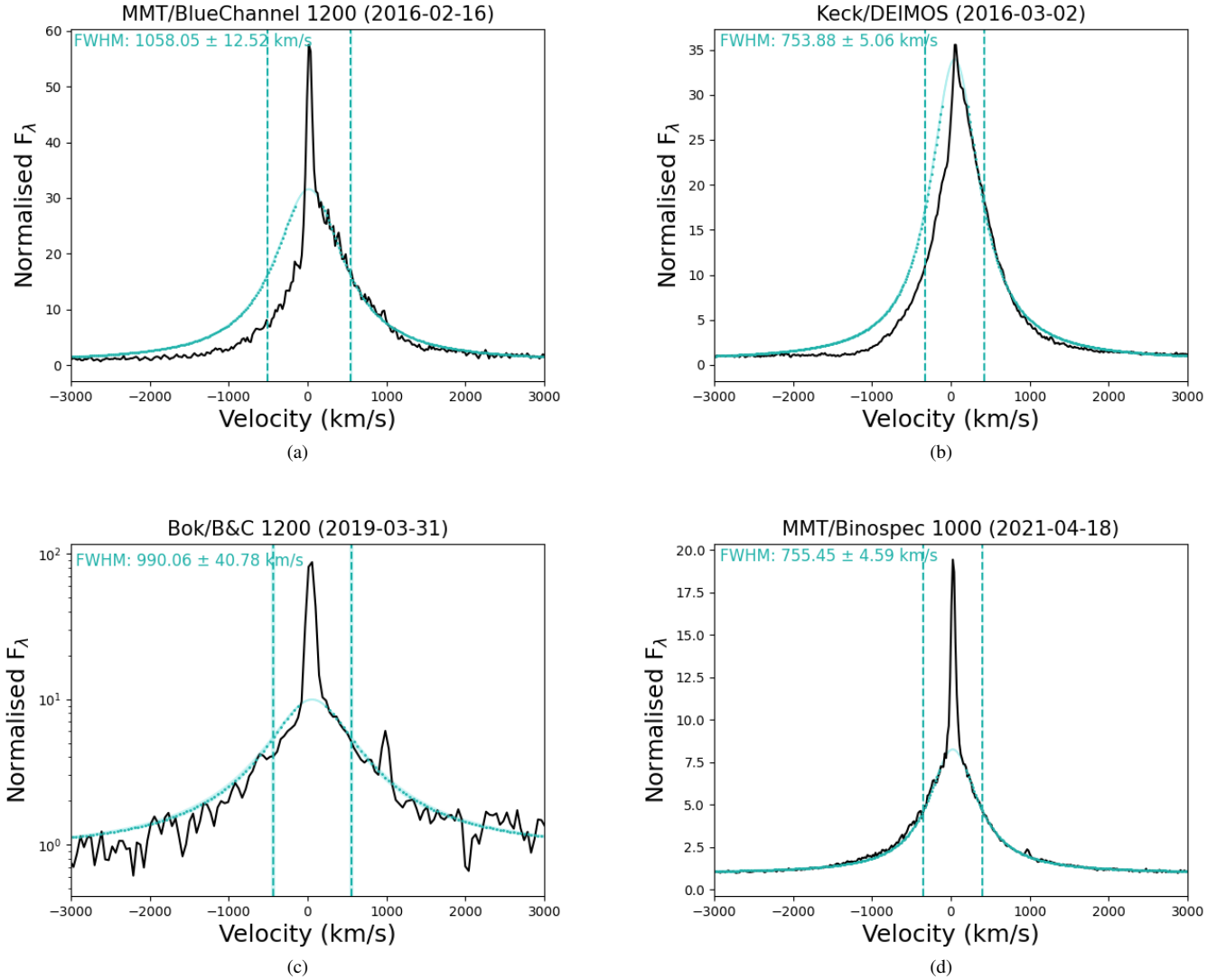


Figure 11. A few $H\alpha$ profiles are overlaid with dotted lines representing the combined Lorentzian and constant-background fits. Owing to contamination from the nearby $H\ II$ region or CSM, we omit the central peak section in our fitting process. Additionally, only the red wings (the redshifted wing reflected over the blue side) are fitted. All the FWHM values, including their corresponding uncertainties, are listed in Table A1.

vary between ~ 300 to 1300 km s^{-1} . In the standard LBV scenario, one might expect slower outflows during brighter states because the star’s radius increases, making it cooler and yielding lower escape velocities. Although there isn’t a strong trend in Fig. 12, brighter states do seem to correlate with slower speeds. Owing to gaps in the photometry data, we are unable to constrain the state of the system during most of the spectroscopic observations (shown with empty symbols). The measured FWHM is sometimes comparable to other LBVs, yet it can reach velocities similar to those observed in SN 2009ip and SN 2000ch. In the next section, we compare the spectra of AT 2016blu with those of SN 2000ch and SN 2009ip.

6 COMPARISON WITH OTHER SN IMPOSTORS

In Fig. 13, we compare the spectra of AT 2016blu with those of other known SN impostors. We have corrected the spectra of both SN 2000ch and SN 2009ip for their respective redshift values, 0.0017

and 0.0059. The spectra of SN 2000ch and the post-outburst (but pre-SN) spectrum of SN 2009ip are also characterised by strong Balmer emission lines with broad wings reaching to high velocities. The spectrum of AT 2016blu includes [S II] and [O III] emission lines, indicative of flux contamination from nearby $H\ II$ regions, which are absent in the spectra of SN 2009ip and SN 2000ch.

During the outburst state, the He I line at 5876 \AA is visible in all spectra; see Fig. 13a. However, the He I line at 6680 \AA is detected in most spectra, but it appears weaker. The Lick/Kast spectrum of AT 2016blu from December 11, 2021, displays Ca II features similar to those observed in SN 2009ip, which are absent in the spectra of SN 2000ch. Similarly, the He II line at 4685 \AA is detected in the 2021 spectra but not in others. It is important to note that these lines are generally observed in the spectra of SN 2000ch (Wagner et al. 2004; Pastorello et al. 2010; Smith et al. 2011).

In the quiescent state, it is much more challenging to detect spectral lines because the targets are usually very faint. For example, while

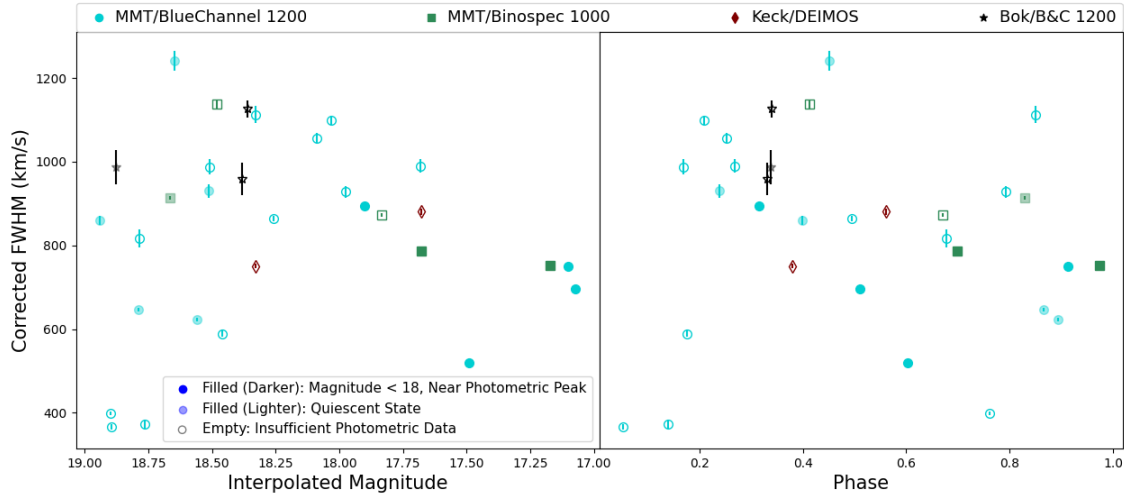


Figure 12. The left and right panels show the FWHM of only high-resolution spectra, after correction for instrumental resolution, versus the interpolated magnitudes at the time the spectra were obtained, and the phase using the 113 d period, respectively. The corrected FWHM for the $H\alpha$ line ranges from ~ 300 to 1300 km s^{-1} . Filled symbols with darker shades represent spectra with an interpolated magnitude brighter than 18 and observed close to the photometric peak, while filled symbols with lighter shades correspond to spectra taken during the quiescent state. Empty symbols represent spectra for which the system’s state could not be determined owing to insufficient photometric data. The shapes and colors indicate different instruments, as noted in the legend. No apparent correlation is found between the FWHM values and the eruptive or quiescent states, nor with the phase.

the He I line at 5876 \AA is visible in all spectra, its presence in the SN 2000ch spectrum observed on 2019-06-04 is difficult to confirm owing to low signal-to-noise ratios. Fig. 13b illustrates that although the higher Balmer lines exhibit a P Cygni profile during an outburst, this feature is less pronounced during the quiescent state.

Fig. 14 shows the velocity profiles for $H\alpha$ from only the high-resolution spectra shown in Fig. 13b. The $H\alpha$ peak in SN 2000ch appears redshifted relative to those of AT 2016blu and SN 2009ip. However, if we disregard the narrow components of AT 2016blu’s $H\alpha$ emission, the broad components of some $H\alpha$ lines sometimes also appear redshifted, similar to SN 2000ch (see Fig. 6). To maintain consistency with the analysis described in Section 5, we exclude the peak of the $H\alpha$ profile from all our fits and only fit the red side of the profile. The corrected Lorentzian FWHM velocities for the broad component of $H\alpha$ are labeled in the figures (see Fig. 14a, and 14b). For the SN 2000ch spectra, which extend to much larger velocities, we applied Lorentzian fits over an extended velocity range (-8000 to 8000 km s^{-1}) to accurately determine the FWHM. SN 2000ch exhibits a notably wider FWHM, consistent with the FWHM reported by Wagner et al. (2004). The FWHM for SN 2000ch is sometimes much larger than that for AT 2016blu. By contrast, the FWHM of SN 2009ip is similar to that of AT 2016blu, regardless of whether the peak is included or excluded.

7 DISCUSSION

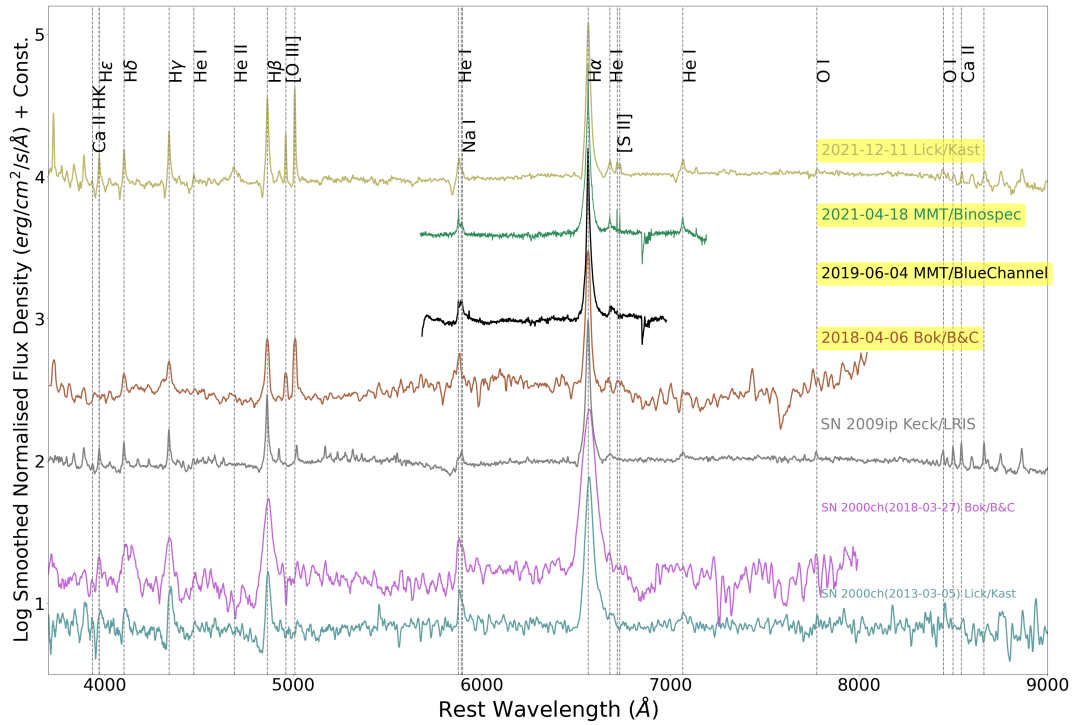
Aghakhanloo et al. (2023b) proposed that AT 2016blu is an eccentric binary system where the primary star is an LBV, and the recurrent outbursts observed in AT 2016blu result from interactions between the two stars during periastron passages. The nature of the companion remains unclear, however. The specific type of binary interaction responsible for the brightening events depends on the companion’s nature and may involve various physical phenomena, such as strong

wind collisions, disc interactions, mass accretion onto a compact object, etc. The spectroscopic analysis of AT 2016blu provides several key insights into this system, beyond what has been inferred from the light curve alone.

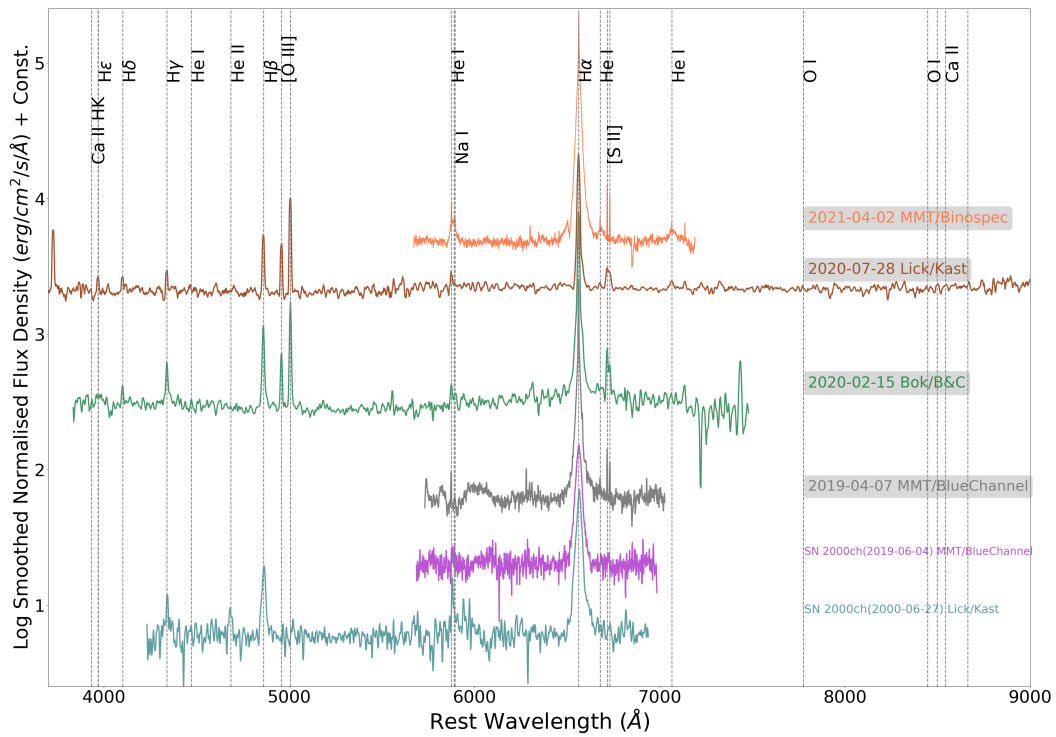
(1) The spectrum of AT 2016blu is different from that of a typical LBV spectrum. The absence of $[\text{Fe II}]$ emission lines, which are often prominent in LBV spectra due to their dense, low-ionisation winds, suggests a different ionisation state or density. AT 2016blu more closely resembles the hottest known LBVs, but it appears to stay hot even in outbursts. In this sense, it is similar to a subset of LBVs like MCA-1b and Romano’s star in M33, and HD 5980 in the SMC (Smith et al. 2020). Additionally, AT 2016blu shows $H\alpha$ FWHM values that are on the high end of the distribution for LBVs (Smith et al. 2011), indicating a relatively fast outflow (or very dense wind; see below) compared to typical LBVs. Hotter stars tend to have faster winds than cooler stars, mostly because cooler stars are also larger and have lower escape speeds. However, other effects like accretion and shock excitation may also play a role here. The presence of these shock waves could result in a higher ionisation state of the gas and might explain the absence of $[\text{Fe II}]$ lines.

(2) The overall spectrum of AT 2016blu remains largely the same over time, with subtle changes. For example, occasional excess flux on the red side of the $H\alpha$ wing, variations in P Cygni features, and the occasional presence of spectral lines like O I , Ca II , and Fe II point to variable conditions within the stellar environment. The P Cygni profiles indicate strong stellar winds and outflows, while the presence of different ionisation states of elements suggests varying temperatures and densities. These observations are consistent with the characteristics of a star that undergoes episodic outbursts and mass ejections.

(3) P Cygni absorption features occasionally appear at very high velocities compared to FWHM estimates for emission components, suggesting that the emission and absorption components are not necessarily tracing the same gas in the outflow. This discrepancy



(a)



(b)

Figure 13. Comparison of normalised spectra from different telescopes during AT 2016blu's outburst and quiescent states, shown in the top and bottom panels, respectively. The spectra of AT 2016blu are compared with those of SN 2000ch, and the post-outburst spectrum of SN 2009ip. The spectrum of SN 2000ch from June 2000 is from [Wagner et al. \(2004\)](#).

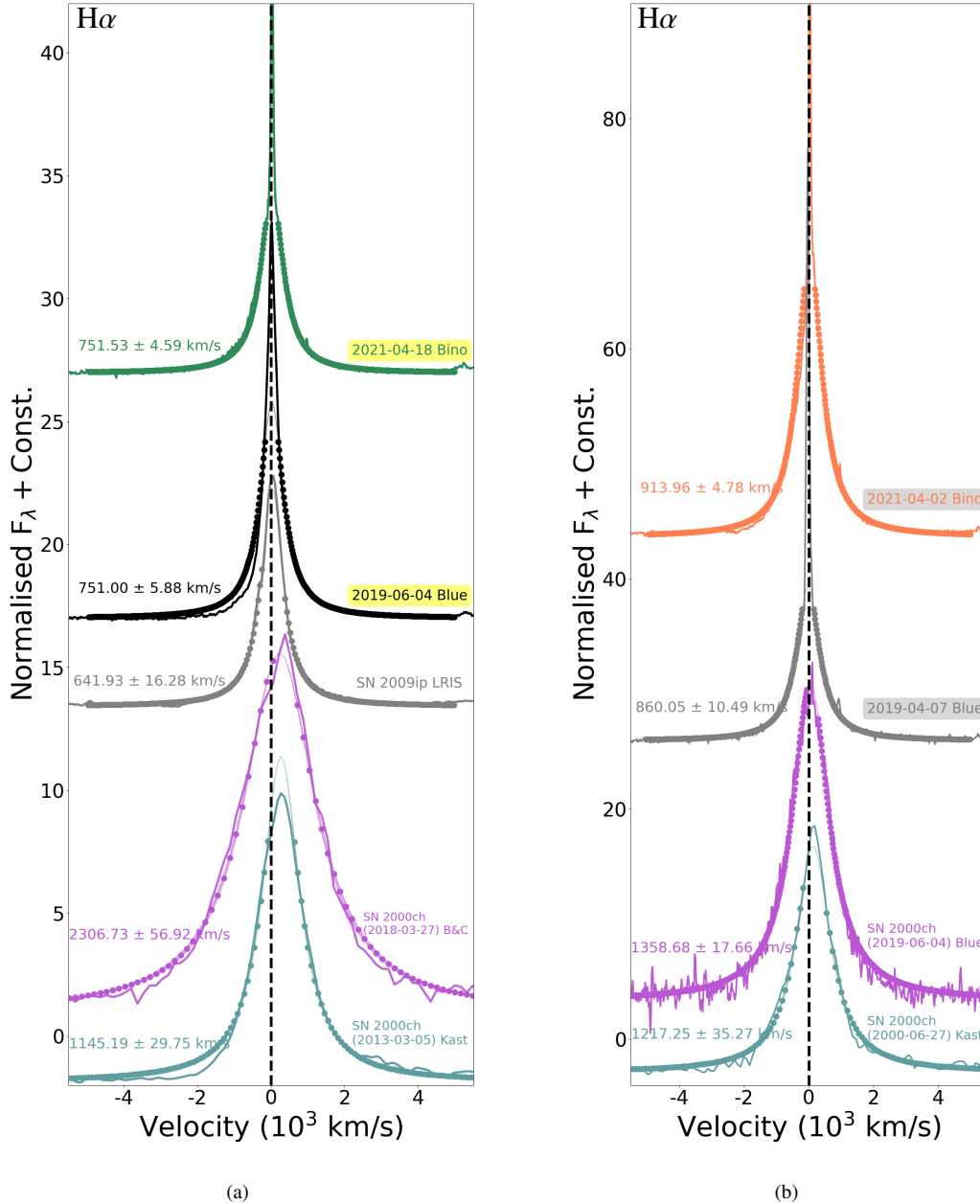


Figure 14. $H\alpha$ velocity profile comparisons of only high-resolution spectra of AT 2016blu with SN 2009ip and SN 2000ch. The $H\alpha$ peak of SN 2000ch is notably redshifted, which is also observed in some spectra of AT 2016blu when the narrow peak is excluded. Lorentzian fits and corrected FWHM estimates are provided for each spectrum. Typically, SN 2000ch exhibits a higher FWHM than AT 2016blu and SN 2009ip. The FWHM of AT 2016blu varies over time, although these variations do not correlate with its eruptive state or 113 d phase.

may indicate the presence of a companion star with a faster outflow, which may be observed in absorption at certain phases. If the system had a purely spherical wind, the emission width should be similar to the absorption width along the line of sight. However, for instance, on 2017-05-20, the $H\alpha$ emission line has an FWHM of around 900 km s^{-1} , while the absorption feature is observed at approximately -4000 km s^{-1} , suggesting a different source or a shock from the fast wind of the companion accelerating material. If due exclusively to a companion, one might expect these features to recur at similar phases in the orbital cycle. Fig. 15 shows the high-resolution $H\alpha$ profiles sorted by magnitude and 113 d orbital phase. No clear correlation is

observed between the high-velocity P Cygni features and either the orbital phase or the magnitude. Fig. 16 also shows a histogram of the orbital phase for all spectra, with spectra exhibiting absorption dips exceeding 2000 km s^{-1} highlighted in yellow. Once again, no correlation is observed, suggesting that these features may not be solely due to the influence of the companion.

(4) While the $H\alpha$ FWHM is commonly interpreted as a direct indicator of wind outflow speed, it is important to consider scenarios where electron scattering plays a dominant role, owing to the fact that the broad component of $H\alpha$ is approximated by a Lorentzian profile shape. If the $H\alpha$ line width is primarily due to electron scat-

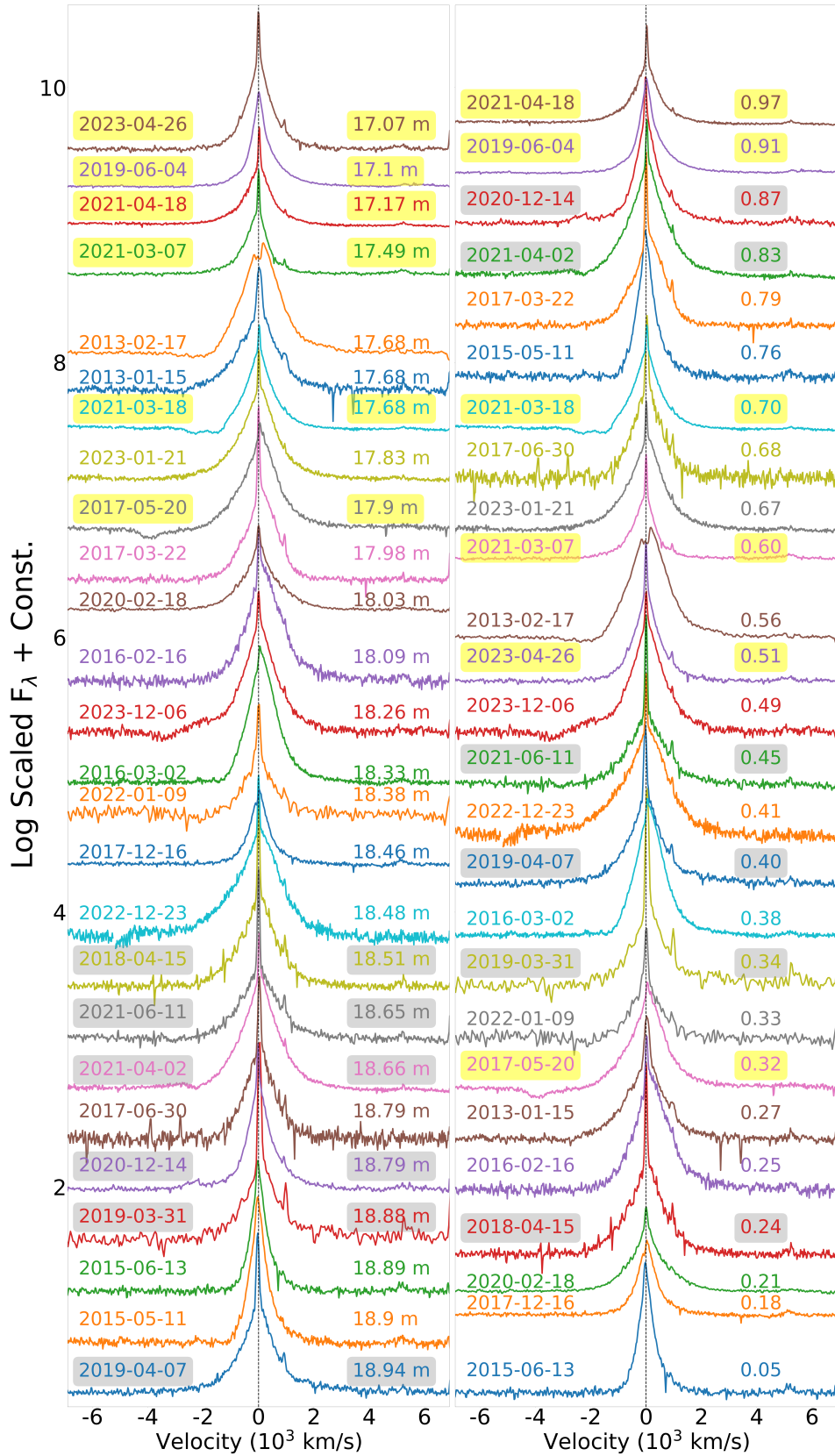


Figure 15. The right and left panels show high-resolution H α profiles organised by magnitude and by 113 d phase, respectively. There is no observed correlation between either the high-velocity P Cygni absorption or the red-side hump features with magnitude or phase. This may suggest an additional component beyond the binary nature of the system, such as the presence of ejected shells.

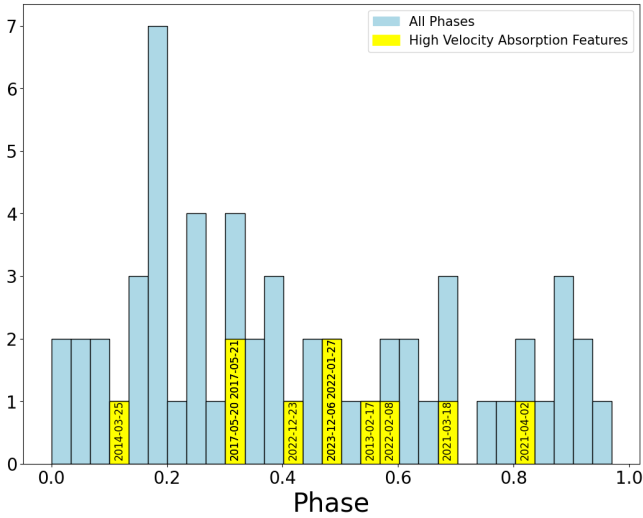


Figure 16. Histogram of the phase using the 113 d period. Spectra with high-velocity absorption dips (greater than 2000 km s^{-1}) are highlighted in yellow. Absorption features are not correlated with the period.

tering, the FWHM may not accurately represent the wind outflow speed (the actual outflow speed would be slower). Instead, the width may be more closely related to the thermal velocities of the electrons responsible for the scattering and the high optical depth of the material. In η Carinae’s current wind, the $H\alpha$ line exhibits a Doppler-broadened core with weaker electron-scattering wings at a mass-loss rate (\dot{M}) of $\sim 1 \times 10^{-3} M_{\odot} \text{ yr}^{-1}$. Given that the Lorentzian profiles in AT 2016blu are persistent throughout its period, this suggests that its mass-loss rate could be even higher than $10^{-3} M_{\odot} \text{ yr}^{-1}$, consistent with the Lorentzian $H\alpha$ line shapes seen in models or early-time spectra of some SNe with strong early CSM interaction (Groh 2014; Shivvers et al. 2015). The persistence of Lorentzian profiles may indicate either a strong steady-state wind from the LBV, or alternatively, high densities in a continuous accretion disc onto a companion star.

(5) Broad P Cygni absorption features sometimes exhibit single troughs and other times double-dip profiles. The presence of an absorption P Cygni feature in the Balmer lines that appears and disappears, and sometimes exhibits a double-dip feature, might be attributed to a variety of phenomena. Changes in the strength and velocity of the stellar wind can cause the absorption feature to vary in intensity and even disappear at times, but the high velocity of these absorption features seems at odds with arising in the LBV’s wind alone, since the outflow speed of the LBV wind should be comparable to or slower than the FWHM values of $H\alpha$ emission. The double-dip feature might occur due to complex wind structures or multiple ejection events with different velocities. In a binary system, if the companion star has a disc, jet, or its own wind, and then this companion passes in front of the LBV, it might also change the observed absorption features. Alternatively, if during an eruption the star ejects mass and forms a dense high-speed shell, it may also be seen in absorption after the eruption.

(6) He I emission lines are detected most of the time, except when the target is faint and the light is dominated by the nearby star cluster rather than the transient. The He I line profile and strength vary significantly over time, often showing multiple peaks, which may result from blending with the Na I line. The presence of both He I + Na I emission lines indicates a wide range of ionisation levels,

perhaps suggesting that accretion luminosity or shocks may add to the stellar photoionisation of the environment within the system.

If the He I lines were due to excitation by colliding wind shocks, one might expect that they should rise as the system approaches periastron and moves into a state of outburst, and should then diminish as the system moves toward apastron. However, we observe that the He I lines are visible at essentially all phases, except for epochs with low signal-to-noise ratio, as noted above. If the He I lines are due instead to an accretion disc around the companion star, then radiative excitation from this accretion might be able to persist longer than the main phase of the visual-wavelength eruption, perhaps lasting for a few months. If the He I line turns on around the time of the outburst, lasts for a while, fades away, and then reappears during the next outburst, it may indicate the influence of an accretion disc. Considering this scenario, we can estimate the accretion luminosity using $L = GM\dot{M}/R$. For an accretion luminosity of $10^6 L_{\odot}$, which would be competitive with the star’s luminosity, and assuming a companion mass $M = 1 M_{\odot}$ and radius $R = 1 R_{\odot}$, we find an accretion rate of $\sim 0.07 M_{\odot} \text{ yr}^{-1}$. This is quite high, suggesting that significant wind mass loss from the primary would be necessary to supply this material. However, the required mass accretion rate could be reduced if the companion is smaller, like a black hole, or significantly more massive.

(7) To better understand this system, we examine how the observed features correlate with the time of periastron. For instance, if the absorption features show no clear correlation with the orbital period, it might indicate that the star is randomly ejecting shells. On the other hand, if these features consistently appear after the main peak (when the magnitude is fainter), it could suggest that more mass is ejected during eruptions. As shown in Fig. 15, there is no clear evidence that the spectral changes are phase-dependent or correlate with the interpolated photometric magnitude. This lack of correlation suggests that additional components beyond the binary interaction may influence the system, such as the presence of ejected shells or clumpy CSM. Interactions between the companion and these dense regions of CSM or shells could produce off-phase features that complicate the observed variability.

We also analyse the radial-velocity variations across the orbital phase. Since the system is likely an eccentric binary, these variations could be attributed to binary motion. Radial velocities were measured by fitting a Lorentzian profile to the broad component of the $H\alpha$ line and correcting for the heliocentric reference frame. To ensure accuracy, we restrict our analysis to high-resolution spectra, where the narrow $H\alpha$ component is well-resolved. This approach allows us to centre the line and minimise the impact of wavelength calibration errors on the observed velocity shifts. As shown in Fig. 17, the heliocentric radial velocities display significant variability. However, this variability does not correlate with the orbital phase, suggesting that other factors might be influencing the observed radial velocities. Alternatively, as suggested in Paper I, AT 2016blu may be less eccentric than SN 2000ch, which could contribute to more erratic radial-velocity behaviour and obscure phase-dependent trends. Another possibility involves stochastic, repeating eruptions from a single star. However, this scenario also faces challenges in aligning with the observations. Such eruptions would likely cause the photosphere to expand and cool or lead to increased mass loss, neither of which have been observed. Furthermore, there is currently no model to explain how this process works or how the star becomes so luminous in such a short time without changing its spectrum.

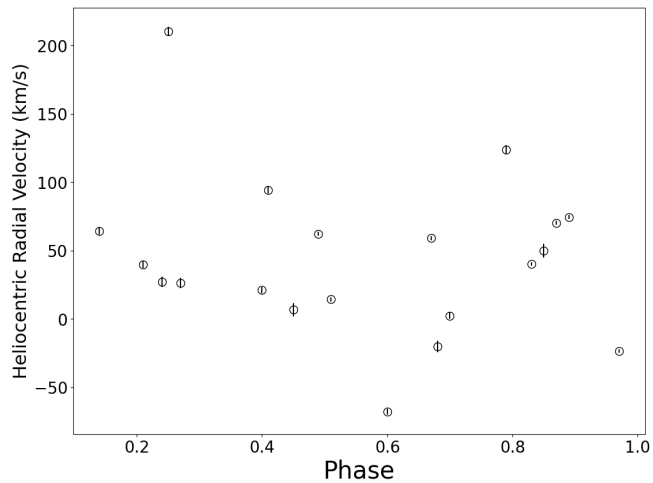


Figure 17. Heliocentric radial velocities for the $H\alpha$ line, derived from high-resolution spectra obtained where the narrow component of the $H\alpha$ profile is resolved. The radial velocities exhibit significant variability but show no correlation with the orbital phase. The lack of a clear pattern suggests that other factors might be influencing the observed radial velocities, or that the variations may not be primarily due to binary motion.

8 CONCLUSION

We present spectroscopic analysis of the SN impostor AT 2016blu, located in an outer spiral arm of NGC 4559. AT 2016blu experienced at least 19 outbursts in 2012–2022, recurring with a period of $\sim 113 \pm 2$ d (Aghakhanloo et al. 2023b). Recent photometric data indicate that AT 2016blu experienced its 20th outburst around May/June 2023, as previously predicted based on its estimated period. These outbursts are suggested to be driven by interactions between two stars near periastron in an eccentric binary system, where the primary star is a massive LBV, and the companion could either be a compact object, such as a neutron star or black hole, or another star.

Our spectroscopic observations, covering multiple outbursts and quiescent states over the past 12 yr, document this transient’s complex behaviour. In general, the spectra of AT 2016blu differ from those of a typical LBV spectrum, instead closely resembling the subset of LBVs that remain hot during eruptions (Smith et al. 2020), including MCA-1B and Romano’s star in M33 and HD 5980 in the SMC. The fact that these remain at a roughly constant temperature as they brighten requires a significant increase in bolometric luminosity, instead of a visual brightening due to redistribution of ultraviolet flux to shorter wavelengths, as usually assumed for LBVs. The AT 2016blu spectra show broad $H\alpha$ profiles with Lorentzian shapes and FWHM values that vary significantly, sometimes much higher than the typical FWHM of LBVs. The higher FWHM suggests the presence of strong stellar winds. Occasionally, broad $H\alpha$ components with asymmetric profiles, featuring a red-side hump, are also observed, indicating self-absorption effects and changes in the density and velocity structure of the stellar wind. Overall, the appearance and behaviour of AT 2016blu’s spectrum closely resemble the spectra of SN impostors like the precursor outbursts of SN 2009ip (Smith et al. 2010) before its 2012 core-collapse event, and also spectra of the SN impostor SN 2000ch (Wagner et al. 2004; Pastorello et al. 2010; Smith et al. 2011), which has very similar recurring periodic outbursts (Aghakhanloo et al. 2023a).

P Cygni absorption features are evident during both outburst and quiescent states, indicating the presence of strong stellar winds and

episodic mass ejections. These features appear as either single or double P Cygni profiles, reaching velocities significantly higher than the FWHM of the emission component of $H\alpha$. This suggests that the absorption component originates from a different source, potentially due to strong winds from the companion star, the presence of dense shells, a jet, or an accretion disc seen along the line of sight to the LBV’s wind.

The He I lines, frequently blended with Na I, are detected in most spectra, indicating the coexistence of hot and cold gas within the system. The persistence of He I throughout most of the orbital period may suggest that excitation of the He I lines is driven by accretion onto the companion object rather than colliding wind shocks.

In conclusion, our study reveals that AT 2016blu is characterised by a complex and dynamic stellar environment, marked by significant spectral variations, strong winds, and interactions within an eccentric binary system. Continued high-cadence photometric and spectroscopic observations over a complete outburst cycle, from the quiescent phase through the peak and back to the end of the cycle, are crucial. Such data would allow for a detailed comparison of the spectral and photometric evolution at each stage of variability, providing deeper insights into the underlying mechanisms driving the recurrent outbursts and further understanding the nature of the companion star in this intriguing transient phenomenon.

ACKNOWLEDGEMENTS

This research has made use of the NASA/IPAC Infrared Science Archive, which is funded by the National Aeronautics and Space Administration (NASA) and operated by the California Institute of Technology. It also used data from the Asteroid Terrestrial-impact Last Alert System (ATLAS) project, which is funded primarily to search for near-Earth objects (NEOs) through NASA grants NN12AR55G, 80NSSC18K0284, and 80NSSC18K1575; byproducts of the NEO search include images and catalogues from the survey area. The ATLAS science products have been made possible through the contributions of the University of Hawaii Institute for Astronomy, the Queen’s University Belfast, the Space Telescope Science Institute (STScI), the South African Astronomical Observatory, and The Millennium Institute of Astrophysics (MAS), Chile. We acknowledge ESA *Gaia*, DPAC, and the Photometric Science Alerts Team (<http://gsaweb.ast.cam.ac.uk/alerts>).

Observations using Steward Observatory facilities were obtained as part of the large observing program AZTEC: Arizona Transient Exploration and Characterization. Some of the observations reported in this paper were obtained at the MMT Observatory, a joint facility of the University of Arizona and the Smithsonian Institution.

Some of the data presented herein were obtained at the W. M. Keck Observatory, which is operated as a scientific partnership among the California Institute of Technology, the University of California, and NASA; the observatory was made possible by the generous financial support of the W. M. Keck Foundation. The authors wish to recognise and acknowledge the very significant cultural role and reverence that the summit of Maunakea has always had within the indigenous Hawaiian community. We are most fortunate to have the opportunity to conduct observations from this mountain. A major upgrade of the Kast spectrograph on the Shane 3 m telescope at Lick Observatory, led by Brad Holden, was made possible through gifts from the Heising-Simons Foundation, William and Marina Kast, and the University of California Observatories. Research at Lick Observatory is partially supported by a generous gift from Google. We thank the staffs at the MMT, Lick, and Keck Observatories for

their excellent assistance. The following people helped with the Lick and/or Keck observations or reductions, for which we are grateful: Brad Cenko, Ori Fox, Melissa Graham, Pat Kelly, Adam Miller, Jeffrey Silverman, and WeiKang Zheng.

Time-domain research by D.J.S. is supported by National Science Foundation (NSF) grants 2108032, 2308181, 2407566, and 2432036 and the Heising-Simons Foundation under grant #2020-1864. A.V.F.'s group at UC Berkeley has received financial assistance from the Christopher R. Redlich Fund, Gary and Cynthia Bengier (S.B.C. was a Bengier Postdoctoral Scholar), William Draper, Timothy and Melissa Draper, Briggs and Kathleen Wood, Sanford Robertson (T.G.B. is a Draper-Wood-Robertson Specialist in Astronomy), and numerous other donors.

DATA AVAILABILITY

ZTF data are available in the public domain <https://irsa.ipac.caltech.edu/Missions/ztf.html>. ATLAS data are available in the ATLAS Forced Photometry server <https://fallingstar-data.com/forcedphot/>. *Gaia* data are available in <http://gsaweb.ast.cam.ac.uk/alerts/home>. The spectroscopic data underlying this article will be shared on reasonable request to the corresponding author.

REFERENCES

- Aghakhanloo M., et al., 2023a, *MNRAS*, **521**, 1941
- Aghakhanloo M., et al., 2023b, *MNRAS*, **526**, 456
- Bellm E. C., et al., 2019, *PASP*, **131**, 068003
- Boian I., Groh J. H., 2018, *A&A*, **617**, A115
- Dedov E., Sarkisyan A., Vinokurov A., Tatarnikov A., Spiridonova O., 2023, *The Astronomer's Telegram*, **16115**, 1
- Elias-Rosa N., et al., 2016, *MNRAS*, **463**, 3894
- Faber S. M., et al., 2003, in Iye M., Moorwood A. F. M., eds, *Society of Photo-Optical Instrumentation Engineers (SPIE) Conference Series Vol. 4841, Instrument Design and Performance for Optical/Infrared Ground-based Telescopes*. pp 1657–1669, doi:10.1117/12.460346
- Fabricant D., et al., 2019, *Publications of the Astronomical Society of the Pacific*, **131**, 075004
- Filippenko A. V., Li W. D., Treffers R. R., Modjaz M., 2001, in Paczynski B., Chen W.-P., Lemme C., eds, *Astronomical Society of the Pacific Conference Series Vol. 246, IAU Colloq. 183: Small Telescope Astronomy on Global Scales*. p. 121
- Gaia Collaboration et al., 2016, *A&A*, **595**, A1
- Groh J. H., 2014, *A&A*, **572**, L11
- Groh J. H., Vink J. S., 2011, *A&A*, **531**, L10
- Groh J. H., Hillier D. J., Daminieli A., Whitelock P. A., Marang F., Rossi C., 2009, *ApJ*, **698**, 1698
- Hillier D. J., et al., 2006, *ApJ*, **642**, 1098
- Kandrashoff M., et al., 2012, *Central Bureau Electronic Telegrams*, **2976**, 1
- Kansky J., et al., 2019, *PASP*, **131**, 075005
- Kashi A., Soker N., 2010, *ApJ*, **723**, 602
- Koenigsberger G., 2004, *Rev. Mex. Astron. Astrofis.*, **40**, 107
- Leitherer C., et al., 1994, *ApJ*, **428**, 292
- Li W. D., et al., 2000, in Holt S. S., Zhang W. W., eds, *American Institute of Physics Conference Series Vol. 522, Cosmic Explosions: Tenth AstroPhysics Conference*. pp 103–106 (arXiv:astro-ph/9912336), doi:10.1063/1.1291702
- Mauerhan J. C., et al., 2013, *MNRAS*, **430**, 1801
- McQuinn K. B. W., Skillman E. D., Dolphin A. E., Berg D., Kennicutt R., 2017, *AJ*, **154**, 51
- Mehner A., et al., 2017, *A&A*, **608**, A124
- Oke J. B., et al., 1995, *PASP*, **107**, 375
- Pastorello A., et al., 2010, *MNRAS*, **408**, 181
- Pastorello A., et al., 2013, *ApJ*, **767**, 1
- Polcaro V. F., et al., 2016, *AJ*, **151**, 149
- Richardson N. D., Morrison N. D., Gies D. R., Markova N., Hesselbach E. N., Percy J. R., 2011, *AJ*, **141**, 120
- Shivvers I., Groh J. H., Mauerhan J. C., Fox O. D., Leonard D. C., Filippenko A. V., 2015, *ApJ*, **806**, 213
- Smith N., 2008, *Nature*, **455**, 201
- Smith N., 2011, *MNRAS*, **415**, 2020
- Smith N., 2014, *ARA&A*, **52**, 487
- Smith N., 2017, *Philosophical Transactions of the Royal Society of London Series A*, **375**, 20160268
- Smith N., Frew D. J., 2011, *MNRAS*, **415**, 2009
- Smith N., et al., 2010, *AJ*, **139**, 1451
- Smith N., Li W., Silverman J. M., Ganeshalingam M., Filippenko A. V., 2011, *MNRAS*, **415**, 773
- Smith N., Mauerhan J. C., Prieto J. L., 2014, *MNRAS*, **438**, 1191
- Smith N., et al., 2018a, *MNRAS*, **480**, 1457
- Smith N., et al., 2018b, *MNRAS*, **480**, 1466
- Smith N., et al., 2020, *MNRAS*, **492**, 5897
- Smith N., Andrews J. E., Filippenko A. V., Fox O. D., Mauerhan J. C., Van Dyk S. D., 2022, *MNRAS*, **515**, 71
- Stahl O., Wolf B., Klare G., Cassatella A., Krautter J., Persi P., Ferrari-Toniolo M., 1983, *A&A*, **127**, 49
- Stahl O., Jankovics I., Kovács J., Wolf B., Schmutz W., Kaufer A., Rivinius T., Szeifert T., 2001, *A&A*, **375**, 54
- Stahl O., Gäng T., Sterken C., Kaufer A., Rivinius T., Szeifert T., Wolf B., 2003, *A&A*, **400**, 279
- Tonry J. L., et al., 2018, *PASP*, **130**, 064505
- Valeev A. F., Vinokurov A., Solovyeva Y., Shablovinskaya E. S., 2021, *The Astronomer's Telegram*, **14638**, 1
- Van Dyk S. D., 2007, *Highlights of Astronomy*, **14**, 205
- Van Dyk S. D., Matheson T., 2012, in Davidson K., Humphreys R. M., eds, *Astrophysics and Space Science Library Vol. 384, Eta Carinae and the Supernova Impostors*. p. 249, doi:10.1007/978-1-4614-2275-4_11
- Vinokurov A., Valeev A. F., Solovyeva Y., 2021, *The Astronomer's Telegram*, **14460**, 1
- Vinokurov A. S., Valeev A. F., Solovyeva Y. N., Aitov V. N., Atapin K. E., Dodin A. V., Tatarnikov A. M., Shatsky N. I., 2022, *The Astronomer's Telegram*, **15808**, 1
- Wagner R. M., et al., 2004, *PASP*, **116**, 326
- van Genderen A. M., 2001, *A&A*, **366**, 508

APPENDIX A: FWHM ESTIMATES

Table A1: Estimated Lorentzian FWHM values for the $H\alpha$ line. These values are presented before correcting for the resolution of each instrument. Measurements are listed by observation date, telescope/instrument used, and the FWHM values in km s^{-1} along with their associated uncertainties.

Date (UT)	Telescope/Instrument	FWHM (km s^{-1})
2013-02-17	Keck/DEIMOS	849 ± 10
2016-03-02	Keck/DEIMOS	884 ± 8
2012-01-18	Lick/Kast	1246 ± 45
2012-02-01	Lick/Kast	1354 ± 54
2014-03-25	Lick/Kast	564 ± 18
2017-05-04	Lick/Kast	1034 ± 57
2020-05-29	Lick/Kast	1332 ± 23
2020-07-28	Lick/Kast	1121 ± 62
2021-12-11	Lick/Kast	777 ± 21
2022-01-27	Lick/Kast	904 ± 57
2022-02-08	Lick/Kast	800 ± 26
2022-06-03	Lick/Kast	1152 ± 27
2012-06-16	Keck/LRIS	897 ± 16
2021-03-18	MMT/Binospec	791 ± 4
2021-04-02	MMT/Binospec	917 ± 5
2021-04-18	MMT/Binospec	755 ± 5
2022-12-23	MMT/Binospec	1141 ± 10
2023-01-21	MMT/Binospec	877 ± 4
2017-01-18	Bok/B&C	470 ± 42
2017-04-17	Bok/B&C	371 ± 24
2017-05-05	Bok/B&C	1048 ± 57
2017-05-14	Bok/B&C	748 ± 21
2018-02-07	Bok/B&C	764 ± 40
2018-04-06	Bok/B&C	441 ± 45
2019-03-14	Bok/B&C	1071 ± 49
2019-03-31	Bok/B&C	990 ± 41
2019-06-06	Bok/B&C	1096 ± 41
2020-01-04	Bok/B&C	950 ± 57
2020-02-15	Bok/B&C	1216 ± 63
2021-04-07	Bok/B&C	1099 ± 67
2022-01-09	Bok/B&C	962 ± 38
2022-01-10	Bok/B&C	1129 ± 21
2023-06-21	Bok/B&C	1052 ± 34
2012-01-30	MMT/BlueChannel	1055 ± 11
2012-01-31	MMT/BlueChannel	990 ± 19
2012-03-02	MMT/BlueChannel	665 ± 7
2012-04-17	MMT/BlueChannel	1114 ± 21
2013-01-15	MMT/BlueChannel	992 ± 16
2015-03-23	MMT/BlueChannel	377 ± 14
2015-05-11	MMT/BlueChannel	404 ± 4
2015-06-13	MMT/BlueChannel	372 ± 6
2016-02-16	MMT/BlueChannel	1058 ± 13
2017-01-07	MMT/BlueChannel	379 ± 11
2017-03-22	MMT/BlueChannel	930 ± 14
2017-05-20	MMT/BlueChannel	896 ± 8
2017-05-21	MMT/BlueChannel	960 ± 14
2017-06-30	MMT/BlueChannel	819 ± 21
2017-12-16	MMT/BlueChannel	593 ± 7
2018-04-15	MMT/BlueChannel	933 ± 16
2019-04-07	MMT/BlueChannel	863 ± 10
2019-06-04	MMT/BlueChannel	754 ± 6
2020-02-18	MMT/BlueChannel	1101 ± 11

Table A1: (continued)

Date (UT)	Telescope/Instrument	FWHM (km s ⁻¹)
2020-12-14	MMT/BlueChannel	650 ± 5
2020-12-17	MMT/BlueChannel	627 ± 4
2021-03-07	MMT/BlueChannel	523 ± 9
2021-06-11	MMT/BlueChannel	1242 ± 24
2023-04-26	MMT/BlueChannel	700 ± 7
2023-12-06	MMT/BlueChannel	867 ± 6

This paper has been typeset from a \LaTeX file prepared by the author.